Ocean Engineering 360 (2026) 125980

Contents lists available at ScienceDirect

Ocean Engineering

journal homepage: www.elsevier.com/locate/oceaneng

Research paper

The influence of different pressure distribution shapes on Kelvin wake based on high order spectral method

Pengju Bao [a], Mingxing Ren [b], Yuan Zhuang [a,*], Decheng Wan [a]

[a] Computational Marine Hydrodynamic Lab (CMHL), School of Ocean and Civil Engineering, Shanghai Jiao Tong University, Shanghai, 200240, China
[b] Ningbo Pilot Station, Ningbo Dagang Pilotage Co., Ltd., Ningbo, 315020, China

ARTICLE INFO

Keywords:
Kelvin wake
High order spectral method
Pressure distribution
Power spectral density

ABSTRACT

Pressure distribution models are widely used to efficiently simulate ship-induced Kelvin waves, yet the impact of their different distribution shapes on wave system characteristics warrants further investigation. A flat-top Gaussian pressure distribution with a broader profile than the standard Gaussian is formulated. The geometric characteristics of the hyperbolic tangent pressure distribution are discussed and compared with those of the Gaussian distribution, revealing its wider spatial extent. The influence of grid resolution on the Kelvin wake system, simulated in HOS-Ocean (a code based on high order spectral method) by introducing a pressure distribution term to approximate the hull-induced free-surface disturbance, is investigated, and a moderate range of grid resolutions is provided. A brief comparative analysis of the effect of different sub-region selections on the power spectral density of the Kelvin wake is also presented. By matching the displaced mass, the drafts corresponding to the two pressure distributions are determined. The resulting wake systems are compared with those obtained using the actual hull draft, providing reference for the selection of draft in practical modeling. Furthermore, Kelvin wakes generated by different pressure distributions under various Froude numbers are calculated and compared. It is found that the hyperbolic tangent pressure distribution demonstrates the capability to generate discernible wave patterns at lower Froude numbers, offering a reference for the study of Kelvin wakes using pressure distribution models.

1. Introduction

When a ship navigates, it generates a Kelvin wake pattern within a wedge-shaped region behind it, characterized by an extensive propagation range and prolonged duration. Within the linear framework, the ship-wave system may be separated into transverse and divergent wave components, allowing the characteristics of each component to be examined individually (Liang et al., 2024). Such a decomposition is helpful for interpreting the structure of the wake pattern and the relative contribution of different wave systems. From an application perspective, the study of ship-generated waves in an Earth-fixed reference frame is also relevant to coastal and environmental protection. As vessel-induced waves propagate toward and along the shoreline, their cumulative action may affect the nearshore hydrodynamic environment and contribute to shoreline erosion. This phenomenon may also pose hazards to moored vessels, and offshore structures (Dam et al., 2008; Dempwolff et al., 2022; Scarpa et al., 2019; Zaggia et al., 2017; Zheng et al., 2023). Moreover, the associated features of the Kelvin wake could reveal information about submerged vehicles such as submarines, including structural dimensions (e.g., hull length) and navigational parameters (e.g., speed and depth) (Arnold-Bos et al., 2007; Gomit et al., 2014; Sun et al., 2018). Therefore, research on the Kelvin wake holds significant practical relevance.

Currently, in the study of Kelvin wakes, a relatively simple approach is to introduce a moving pressure distribution term into the dynamic free surface boundary condition (DFSBC) based on potential flow theory, aiming to approximate the disturbance induced by a navigating ship on the free surface. By simplifying a ship to a moving "point pressure" source on the free surface and based on the assumption of infinite water depth, Kelvin (1887) first theoretically proposed and predicted the extent of the wedge-shaped region, known as the famous Kelvin angle, $\theta_{Kelvin} = 19.28^{\circ}$. Although a single point pressure source can reasonably describe the basic characteristics of the wave system, it fails to account for the important variations of these characteristics with the parameters of the moving body. For this point-source model, θ_{Kelvin} is a constant, independent of the Froude number Fr, whereas in reality, this value is

* Corresponding author.
E-mail address: nana2_0@sjtu.edu.cn (Y. Zhuang).

https://doi.org/10.1016/j.oceaneng.2026.125980
Received 24 February 2026; Received in revised form 27 April 2026; Accepted 6 May 2026
Available online 18 May 2026

closely related to factors such as speed, hull dimensions, water depth, and even submerged depth (for submarine). Building upon Kelvin's work, Havelock (1908) replaced the ship with a pressure disturbance of uniform strength distributed over a finite circular area, obtaining the morphology of the wave system under different water depths, where the wave angle varies with water depth. Honger (1923) further substituted the ship with a more complex distribution of moving pressure disturbances along the water surface, deriving the wave height expression for infinite water depth.

Doctors and Sharma (1972) employed a hyperbolic tangent pressure distribution to model the hull, and investigated the theoretical wave resistance of an Air Cushion Vehicle (ACV) under various water depths and both steady and unsteady motion conditions using its limiting case of a rectangular distribution. Building upon this, Doctors (1993) further refined the pressure distribution term, deriving a smoothed-edge hyperbolic tangent pressure distribution. Ertekin et al. (1986) utilized the Green-Naghdi equations, replacing ship motion with a steadily moving, centrally symmetric rectangular pressure patch, to achieve numerical simulation of the wake field in a shallow-water channel.

Furthermore, the Gaussian distribution is frequently applied in the investigation of Kelvin wake thanks to its favorable geometric properties. Rabaud and Moisy (2013) approximated the hull using an axisymmetric Gaussian pressure distribution model, with numerical calculations confirming that the wake angle appears inversely proportional to the ship's speed at high velocities. Darmon et al. (2014) further investigated the wake system at high hull-based Froude numbers and demonstrated that the angle corresponding to the maximum wave height is inversely proportional to the Froude number, while the overall wake remains confined within the classical Kelvin angle. Based on this phenomenon, Pethiyagoda et al. (2014) introduced the concept of the apparent wake angle and a method for its determination, proving that nonlinear effects tend to increase this apparent angle. Benzaquen et al. (2014) used an elliptical Gaussian pressure distribution to better represent the geometric anisotropy of real hulls and examined wake characteristics and wave resistance at various Froude numbers. Moisy and Rabaud (2014) extended their previous study to non-axisymmetric pressure distributions, studying the effect of the distribution's aspect ratio on the far-field maximum wave height. Paprota (2023) extended the approach by simplifying hulls of given geometry into a sum of two-dimensional (2D) Gaussian functions to simulate multi-hull vessels.

Due to the smooth head and tail profiles of a Gaussian pressure distribution, along with its concentration of pressure near the center, it may not adequately characterize the abrupt geometric variations at the bow and stern of a real ship hull. Lo (2021) compared the wave systems generated by rectangular and Gaussian pressure distributions, indicating that real hull wakes fall between these extremes. Bao et al. (2026) improved upon the conventional Gaussian pressure distribution by extending the pressure distribution outward from the center toward both sides, and found that it could generate more distinct bow and stern wave systems.

Given that Gaussian and hyperbolic tangent pressure distributions are commonly employed in current studies, this paper will further investigate and compare their similarities and differences, aiming to provide insights for the study of Kelvin wake systems. It is noteworthy that the pressure distribution typically employed is the hydrostatic pressure exerted by the stationary hull on the free surface. However, when the hull is in motion, the pressure on its surface deviates from the hydrostatic value. Yao et al. (2024) introduced a dynamic pressure correction strategy to accurately simulate the influence of ship motion on the hull surface pressure, although this effect is not considered in the present study.

A more precise representation of ship-generated wave patterns employs the Green function method, which enables the exact satisfaction of boundary conditions on the wetted surface of a submerged or partially submerged hull (Brard, 1972; Chen et al., 2019; Dawson, 1977; Forbes, 1989; Gadd, 1976; He et al., 2016; Kotchin, 1951; Ma et al., 2016; Noblesse, 1977; Pethiyagoda et al., 2021; Zhang et al., 2015; Zhu et al., 2018). A further and more accurate description involves the use of computational fluid dynamics (CFD) methods. However, owing to limitations in computational domains and boundaries, traditional numerical methods are unable to effectively and efficiently compute the complete Kelvin wake system in open ocean. The high order spectral (HOS) method (Dommermuth and Yue, 1987; West et al., 1987) exhibits extremely fast convergence when solving wave problems and has been extensively studied by numerous researchers to date (Fouques and Pákozdi, 2020; Gouin et al., 2017; Gramstad et al., 2023; Guyenne, 2017; Kirezci et al., 2021, and so on). Among these, the open-source software HOS-Ocean (a code based on HOS method), developed by Ducrozet et al. (2016), can effectively simulate wave evolution in open ocean but does not account for the presence of objects and thus cannot generate Kelvin wakes. By introducing a Gaussian pressure distribution, Bao et al. (2025) enabled the evolution of Kelvin wakes, thereby extending the application scope of HOS-Ocean. While Kelvin wave theory and related numerical approaches are well established, the pressure distribution method remains an efficient and practically useful framework for ship-wave generation. Compared with CFD-based ship-resolving simulations and potential-flow methods such as Green-function or boundary element methods, it provides a computationally economical way to generate the primary free surface wave induced by a moving ship. This advantage is particularly valuable when combined with the HOS approach for large-domain wake simulations.

Nevertheless, several issues warrant consideration when employing such computational approach. On one hand, the method is based on HOS method, a pseudo-spectral approach that relies on the Fast Fourier Transform (FFT) for calculation. Consequently, the number of grids corresponds directly to the number of spectral modes, which fundamentally limits the maximum wavenumber that can be represented in the generated wave system. Colen and Kolomeisky (2021) demonstrated the existence of two characteristic Froude numbers for the Kelvin wake system, classified the wake patterns, and examined the influence of different maximum wavenumbers on the structure of the Kelvin wake. Different maximum wavenumbers correspond to distinct Kelvin wake structures, implying that the Kelvin wake patterns calculated under different grid resolutions may vary. So, it is necessary to investigate the capability of HOS-Ocean in simulating Kelvin wakes under varying grid resolutions. Furthermore, unlike wave generation in an empty domain, when introducing a pressure distribution term, the influence of mesh resolution on the shape of the pressure distribution must also be considered. For instance, in the case of a Gaussian pressure distribution, which is smooth and flat at both ends, whether there exists a reasonable range of mesh densities sufficient to adequately resolve its shape, thereby relatively accurately generating the Kelvin wake pattern. For a computational domain of fixed size, employing a finer grid resolution enables the capture of more detailed wave information and pressure distribution feature, albeit at the cost of increased computational time. Whether an optimal relationship between computational domain size and grid resolution can be identified to maintain computational efficiency while ensuring result reliability. Bao et al. (2025) conducted a preliminary study on this topic, focusing primarily on the comparison of free-surface elevation at specific locations, without exploring the variations in the shape of the pressure distribution or the structure of the Kelvin wave pattern. Therefore, one of the objectives of this study is to further investigate the influence of different grid resolutions in HOS-Ocean on pressure distribution shape and the simulation results.

On the other hand, when employing a pressure distribution, it is typically represented by both a shape factor and a peak factor. The peak factor, which is proportional to the draft, is usually determined by ensuring that the equivalent pressure representing the actual displacement volume of the ship is equal to the spatial integral of the pressure distribution (Doctors, 1993; Lo, 2021; Yao et al., 2024). Another approach is to use the average or maximum draft of the actual hull directly (Paprota, 2023), and both methods can generate reasonable Kelvin wake patterns. However, a key issue arises: the draft value obtained through matching displacement volume may be higher or lower than the actual hull draft, thereby influencing the results of the Kelvin wake system. Therefore, for a given pressure distribution, a comparative analysis is required to examine the differences in draft resulting from different draft determination methods and their subsequent impact on the Kelvin wake pattern. Similarly, for different pressure distributions, due to different mathematical properties, when the same draft determination method (i.e. by matching displacement volume) is applied to establish the draft, the differences in the resulting draft, as well as their influence on the Kelvin wake pattern, should be investigated. Accordingly, one of the objectives of this study is to analyze the geometric characteristics of different pressure distributions and to investigate the impact of draft on the wake system. In addition, preliminary computations of the Kelvin wake systems for these two different pressure distributions at various Froude numbers were performed, followed by a comparative analysis of their similarities, differences, and respective capabilities in generating the wake patterns.

In short, the present study goes beyond simply adopting an existing pressure model. First, a flat-top Gaussian pressure distribution is introduced in addition to the standard Gaussian form used in earlier work. This allows a broader effective pressure distribution and leads to clearer bow and stern wake structures. Second, the mathematical properties of Gaussian and hyperbolic tangent pressure distributions are compared systematically, and the corresponding draft-selection methods are discussed. Third, the computational capability of HOS-Ocean for wake simulation based on pressure distribution is examined through the influence of grid resolution on both pressure representation and Kelvin wake prediction. The contribution of the paper therefore lies in improving the modeling basis and practical use of pressure-distribution methods within an HOS framework, rather than in reusing a simplified assumption alone.

In Section 2, the governing equations of the High-Order Spectral (HOS) method, the basic forms of the Gaussian and hyperbolic-tangent pressure-distribution terms, and their geometric characteristics are introduced. In section 3, the influence of the HOS-Ocean grid resolution on wake generation is firstly examined; a brief comparison is then made regarding the effect of sub-region selection on the power spectral density representation of the Kelvin wake, followed by a discussion of the determination of the pressure distribution draft and its impact on the wave system. Finally, preliminary computations of Kelvin wakes generated by different pressure distributions under various Froude numbers are presented and compared. Conclusions and an outlook are provided in Section 4.

2. Numerical methods

2.1. High order spectral method

Within the framework of potential theory, the fluid is assumed to be incompressible, inviscid, and the flow irrotational; therefore, a velocity potential ϕ can be employed. For water waves, the system satisfies the Laplace equation (Eq. (1)) and the free surface boundary conditions (FSBC) (Eqs. (2) and (3)):

$$\Delta\phi = \nabla_{\mathbf{x}}^2\phi + \partial_z^2\phi = 0 \tag{1}$$

$$\eta_t + \nabla_{\mathbf{x}}\phi\cdot\nabla_{\mathbf{x}}\eta - \partial_z\phi = 0 \quad z = \eta \tag{2}$$

$$\phi_t + g\eta + \frac{1}{2}\left[(\nabla_{\mathbf{x}}\phi)^2 + (\partial_z\phi)^2\right] + \frac{P}{\rho} = 0 \quad z = \eta \tag{3}$$

where $\mathbf{x} = (x, y)$ represents the horizontal coordinates, while z denotes the vertical direction; ∇ is the spatial gradient operator (the operator $\nabla_{\mathbf{x}}^2$ includes both horizontal directions, namely $\nabla_{\mathbf{x}}^2\phi = \partial_x^2\phi + \partial_y^2\phi$), and the subscript t indicates the partial derivative with respect to time; $\eta(\mathbf{x}, t)$ and $\phi(\mathbf{x}, t)$ are functions of both space and time, representing the free-surface elevation and the velocity potential, respectively; g is the gravitational acceleration, P denotes the pressure at the free surface, and ρ is the fluid density.

The high order spectral (HOS) method is based on the pseudo-spectral approach and aims to solve for the velocity potential that satisfies the Laplace equation. By considering only the velocity potential on the horizontal directions and referring to Zakharov (1972), the surface velocity potential ϕ^s is introduced:

$$\phi^s(\mathbf{x}, t) = \phi(\mathbf{x}, \eta(\mathbf{x}, t), t) \tag{4}$$

Taking the time derivative and the spatial gradient in the horizontal directions of the surface velocity potential, and assuming that ϕ and η are $O(\epsilon)$, where the wave steepness $\epsilon = kA$ must be much smaller than 1 (with k being the wavenumber and A the wave amplitude), ϕ is expanded via a perturbation series. A Taylor expansion is performed about $z = 0$, retaining terms up to the same order M.

$$\phi^s(\mathbf{x}, t) = \phi(\mathbf{x}, \eta, t) = \sum_{m=1}^{M}\sum_{k=0}^{M-m}\frac{\eta^k}{k!}\frac{\partial^k}{\partial z^k}\phi^{(m)}(\mathbf{x}, 0, t) \tag{5}$$

Through mode matching, the velocity potential at each order is expressed using eigenfunction $\psi_n(\mathbf{x}, z)$.

$$\phi^{(m)}(\mathbf{x}, z, t) = \sum_{n=1}^{\infty}\phi_n^{(m)}(t)\psi_n(\mathbf{x}, z) \tag{6}$$

By truncating at the appropriate number of modes N, the vertical velocity W at the free surface can be obtained:

$$W = \partial_z\phi(\mathbf{x}, \eta, t) = \sum_{m=1}^{M}\sum_{k=0}^{M-m}\frac{\eta^k}{k!}\sum_{n=1}^{N}\phi_n^{(m)}(t)\frac{\partial^{k+1}}{\partial z^{k+1}}\psi_n(\mathbf{x}, 0) \tag{7}$$

Consequently, these yield the kinematic free surface boundary condition (KFSBC) and dynamic free surface boundary condition (DFSBC) (as Eqs. (8) and (9), respectively) within HOS method.

$$\eta_t + \nabla_{\mathbf{x}}\phi^s\cdot\nabla_{\mathbf{x}}\eta - (1 + \nabla_{\mathbf{x}}\eta\cdot\nabla_{\mathbf{x}}\eta)\left[\sum_{m=1}^{M}\sum_{k=0}^{M-m}\frac{\eta^k}{k!}\sum_{n=1}^{N}\phi_n^{(m)}(t)\frac{\partial^{k+1}}{\partial z^{k+1}}\psi_n(\mathbf{x}, 0)\right] = 0 \tag{8}$$

$$\phi_t^s + g\eta + \frac{1}{2}\nabla_{\mathbf{x}}\phi^s\cdot\nabla_{\mathbf{x}}\phi^s - \frac{1}{2}(1 + \nabla_{\mathbf{x}}\eta\cdot\nabla_{\mathbf{x}}\eta)\left[\sum_{m=1}^{M}\sum_{k=0}^{M-m}\frac{\eta^k}{k!}\sum_{n=1}^{N}\phi_n^{(m)}(t)\frac{\partial^{k+1}}{\partial z^{k+1}}\psi_n(\mathbf{x}, 0)\right]^2 + \frac{P}{\rho} = 0 \tag{9}$$

In the present computation, Eqs. (8) and (9) are solved in a time-marching manner within the HOS-Ocean framework. The free-surface elevation η and surface potential ϕ^s are taken as the primary unknowns. At each time step, their horizontal spatial derivatives are evaluated using the pseudo-spectral HOS discretization, and the free-surface vertical velocity W is then obtained. The pressure term is introduced into the dynamic free-surface boundary condition as an external forcing. To represent a ship moving at constant speed, an equivalent-inflow formulation is adopted: a uniform incoming flow is imposed relative to a stationary pressure distribution, which is physically equivalent to a pressure distribution translating steadily over calm water. The resulting time derivatives η_t and ϕ_t^s are integrated using an adaptive-time-step, six-stage, fifth-order (fourth-order) Runge–Kutta method, details refer to Ducrozet et al. (2016).

2.2. Pressure distribution term

The pressure distribution P is used to approximate the disturbance induced by the ship hull on the free surface, and its introduction into DFSBC enables the generation and evolution of the Kelvin wake. In the present study, the pressure distribution is essentially a simplified equivalent model used to represent the overall disturbance induced by the hull on the free surface, rather than a pointwise reconstruction of the actual hull-surface pressure. Its correlation with the ship hull is established through the principal dimensions (the horizontal extent of the pressure patch is determined by the ship length and beam), the draft-dependent pressure magnitude, and the displaced-mass matching used to ensure equivalent displaced volume.

In principle, one may consider using pressure information that is closer to the real hull surface. However, within the HOS framework, the governing variables are defined on the free surface, and the pressure term must be imposed as a single-valued distribution on the free surface, i.e., each horizontal location corresponds to only one pressure value. This is not fully compatible with real three-dimensional hull geometries containing features such as a bulbous bow or other locally overhanging structures. In addition, adopting a more realistic and geometrically complex pressure field would introduce sharper spatial variations, which would substantially increase the grid-resolution requirement in HOS, leading to higher computational cost and potentially additional numerical stability issues.

For this reason, the present study employs parameterized pressure distributions constrained by the ship length, beam, draft, and displaced mass, so as to achieve a practical balance between computational efficiency, numerical robustness, and physical relevance. It should be noted that the pressure distribution corresponds to a stationary hull, with hull motion represented by the translation of the pressure distribution. Dynamic pressure correction (Yao et al., 2024) is not considered in this paper.

Let $\boldsymbol{x} = (x, y)$ and $\boldsymbol{u} = (U, V)$ denote the horizontal coordinates and velocity vector, respectively, and the general form of the pressure distribution P is given by Eq. (10).

$$P = P(\boldsymbol{x}, t) = P(\boldsymbol{x} - \boldsymbol{u}t) \tag{10}$$

Further considering, the pressure distribution is assumed to be the product of a peak pressure factor $P_0 = \rho g D_s$, and a shape function $S(\boldsymbol{x}, t)$:

$$P(\boldsymbol{x}, t) = P_0 \cdot S(\boldsymbol{x}, t) = \rho g D_s \cdot S(\boldsymbol{x} - \boldsymbol{u}t) \tag{11}$$

where $S(\boldsymbol{x}, t)$ is a shape distribution with a peak value of 1. Its form can be either a mathematical expression or a series of discrete data points from real hull. In this paper, two different types of pressure distribution functions are selected: the Gaussian pressure distribution and the hyperbolic tangent pressure distribution. D_s denotes the draft, whose value can be either the actual hull draft or be determined by ensuring that the displaced liquid volume of the adopted pressure distribution equals that of the actual hull (as Eq. (12)).

$$\frac{m}{\rho} = \iint D_s \cdot S(\boldsymbol{x}, t) \mathrm{d}\boldsymbol{x} = D_s \cdot \mathrm{I} \tag{12}$$

where m denotes the actual displacement mass of the hull, and $I = \iint S(\boldsymbol{x}, t) \mathrm{d}\boldsymbol{x}$ is the spatial integral of the shape function $S(\boldsymbol{x}, t)$.

2.2.1. Gaussian pressure distribution

Consider the ship length L_s, beam B_s, and then the general expression of the Gaussian distribution function is first provided, i.e., Eq. (13). Its characteristic is that the pressure distribution is concentrated near the center.

$$S_{G1}(x, y) = \exp\left(-\beta \left(\frac{(x - \mu_x)^2}{L_s^2} + \frac{\left(y - \mu_y\right)^2}{B_s^2} \right) \right) \tag{13}$$

where μ_x and μ_y represent the coordinates of the peak center of the shape function $S(x,y)$, $\beta = 4\, log(a)$ represents the shape parameter and $a > 1$ is a constant denoting peak ratio. Further details can be found in Bao et al. (2025).

Bao et al. (2026) further improved upon $S_{G1}(x, y)$ by modifying the pressure distribution so that it is no longer concentrated solely near the center but can extend toward both sides, thereby better simulating the abrupt changes in the bow and stern geometry of a real hull, as is shown in $S_{G2}(x, y)$.

$$S_{G2}(x, y) = \exp\left(-\left(\beta_x \cdot \left(\frac{x - \mu_x}{L_s} \right)^{n_x} + \beta_y \cdot \left(\frac{y - \mu_y}{B_s} \right)^{n_y} \right) \right) \tag{14}$$

where $\beta_x = 2^{n_x} \log(a_x)$ and $\beta_y = 2^{n_y} \log(a_y)$ denote the longitudinal and transverse decay coefficients, respectively, while n_x and n_y represent the corresponding exponential factors. Within this formulation, it is conventionally recommended that the exponent n_x and n_y be even integers to ensure favorable mathematical properties. In the present study, the model is further generalized by allowing n to take any real number greater than 1, as shown in Eq. (15).

$$S_{G3}(x, y) = \exp\left(-\left(\beta_x \cdot \left| \frac{x - \mu_x}{L_s} \right|^{n_x} + \beta_y \cdot \left| \frac{y - \mu_y}{B_s} \right|^{n_y} \right) \right) \tag{15}$$

For this pressure distribution representation, the effective hull length and beam are defined at the positions where the distribution attains the value $1/a_x$ and $1/a_y$, respectively. As shown in Fig. 1, the pressure distribution becomes notably more rectangular and is no longer confined to a small region near the center. It is evident that the pressure distribution expressed in Eq. (15) can represent bow-stern asymmetry. And when $n_x = n_y = 2$ and $\beta_x = \beta_y$, the expression reduces to Eq. (13) (so called standard Gaussian distribution, here).

2.2.2. Hyperbolic tangent pressure distribution

Another pressure distribution function examined in this paper is the hyperbolic tangent, whose basic form is given by:

$$\begin{aligned} S_{H1}(x, y) = 0.25 \cdot & \left(\tanh\left(\alpha_1 \left(x + \frac{L_s}{2} \right) \right) - \tanh\left(\alpha_2 \left(x - \frac{L_s}{2} \right) \right) \right) \\ & \cdot \left(\tanh\left(\alpha_3 \left(y + \frac{B_s}{2} \right) \right) - \tanh\left(\alpha_4 \left(y - \frac{B_s}{2} \right) \right) \right) \end{aligned} \tag{16}$$

where α_1 and α_2, as well as α_3 and α_4, are shape coefficients controlling the longitudinal and lateral steepness, respectively. When these coefficients are equal respectively, the distribution becomes symmetric. It can be known that the values of α may cause the peak of the distribution function to deviate from 1. Therefore, it is necessary to consider the lower bound for α when the peak value approaches 1. For ease of discussion, let $\alpha_1 = \alpha_2 = \alpha_x$ and $\alpha_3 = \alpha_4 = \alpha_y$, meaning that both the longitudinal and lateral sides are symmetric, respectively. Eq. (16) can then be rewritten as:

$$\begin{aligned} S_{H2}(x, y) = 0.25 \cdot & \left(\tanh\left(\alpha_x \left(x + \frac{L_s}{2} \right) \right) - \tanh\left(\alpha_x \left(x - \frac{L_s}{2} \right) \right) \right) \\ & \cdot \left(\tanh\left(\alpha_y \left(y + \frac{B_s}{2} \right) \right) - \tanh\left(\alpha_y \left(y - \frac{B_s}{2} \right) \right) \right) \end{aligned} \tag{17}$$

The considered shape distribution exhibits an analogous form in both the longitudinal and transverse directions. Then, the longitudinal distribution $S_H(x)$ is extracted here to examine its mathematical properties.

$$S_H(x) = 0.5 \cdot \left(\tanh\left(\alpha_x \left(x + \frac{L_s}{2} \right) \right) - \tanh\left(\alpha_x \left(x - \frac{L_s}{2} \right) \right) \right) \tag{18}$$

Fig. 1. Schematic diagram of the Gaussian pressure distribution described by Eq. (15), where $n_x = n_y = n = 3$ and $\beta_x = \beta_y = 2^n \log(a)$, $a = 7.39$ (the value of a is same as which in Lo (2021)). (a) Three-dimensional view; (b) top view: the central white area shows the characteristics of the platform.

Table 1
Peak values corresponding to different values of $\alpha_x L_s/2$.

$\alpha_x L_s/2$	1.0	1.5	2.0	3.0	4.0	5.0
$S_H(x=0)$	0.7616	0.9051	0.9640	0.9951	0.9993	0.9999

Differentiation of Eq. (18) reveals that the peak value is located at the center, i.e., $S_H(x=0) = \tanh(\alpha_x L_s/2)$. The function approaches unity only when $\alpha_x L_s/2$ is sufficiently large.

As shown in Table 1, several specific values are provided. When $\alpha_x L_s/2 < 3.0$, the peak value gradually deviates from unity. For $\alpha_x L_s/2 = 5$, the value closely approaches 1. This indicates that to ensure the peak remains near unity, the practical lower bound for $\alpha_x L_s/2$ lies between 3 and 5. Evidently, if the value of $\alpha_x L_s/2$ is given, when L_s varies, the lower bound for α_x changes accordingly. Here, to facilitate discussion, it is treated as a combined term by defining $\alpha_x L_s = \alpha_{xs}$, and then the lower bound becomes $\alpha_{xs} \geq 6$. Similarly, let $\alpha_y B_s = \alpha_{ys}$. Thereby Eq. (18) can then be rewritten as Eq. (19), which depends only on a given set of values and is no longer influenced by the specific hull dimensions.

$$S_{H3}(x,y) = \frac{1}{4}\cdot\left(\tanh\left(\alpha_{xs}\left(\frac{x}{L_s}+\frac{1}{2}\right)\right) - \tanh\left(\alpha_{xs}\left(\frac{x}{L_s}-\frac{1}{2}\right)\right)\right) \cdot\left(\tanh\left(\alpha_{ys}\left(\frac{y}{B_s}+\frac{1}{2}\right)\right) - \tanh\left(\alpha_{ys}\left(\frac{y}{B_s}-\frac{1}{2}\right)\right)\right) \tag{19}$$

Comparing Figs. 1 and 2, it is apparent that the hyperbolic tangent pressure distribution appears wider and more closely approximates a

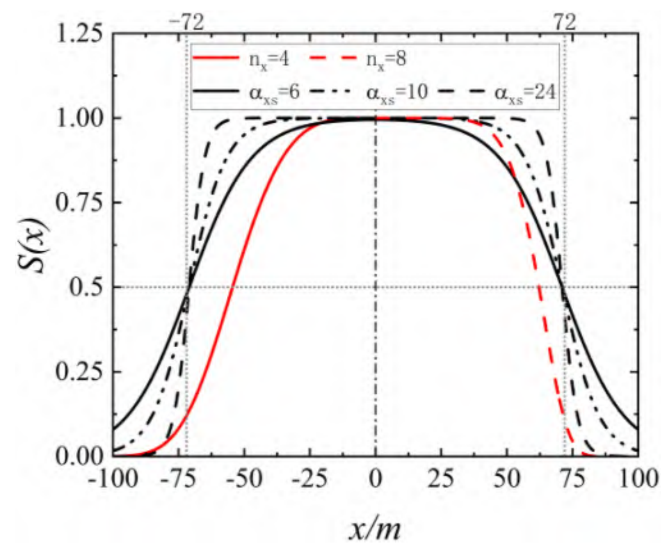

Fig. 3. Comparison of the longitudinal profiles of the Gaussian pressure distribution and the hyperbolic tangent pressure distribution. Red lines: Gaussian pressure distribution with $a = 7.39$ and different values of $n_x = 4, 8$; Black lines: hyperbolic tangent pressure distribution with different values of $\alpha_{xs} = 6, 10, 24$. (For interpretation of the references to color in this figure legend, the reader is referred to the Web version of this article.)

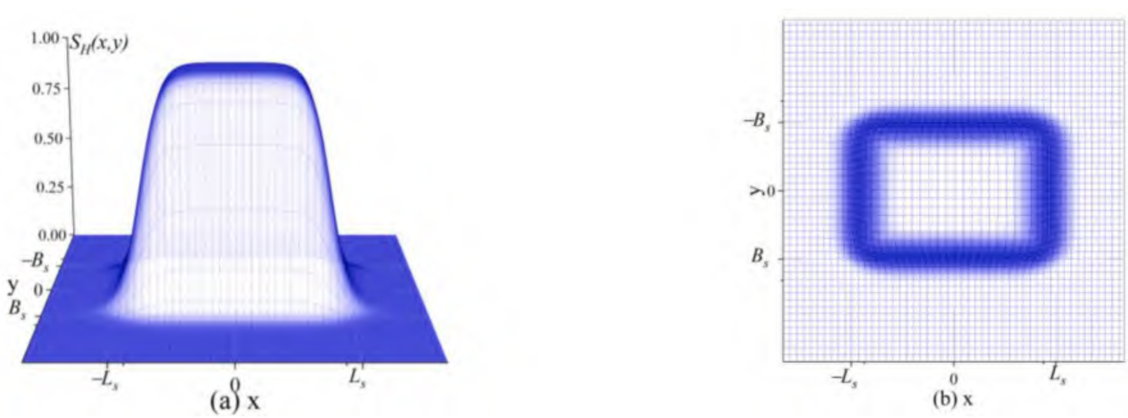

Fig. 2. Schematic diagram of the hyperbolic tangent pressure distribution described by Eq. (19), where $\alpha_{xs} = \alpha_{ys} = 10$. (a) Three-dimensional view; (b) top view: the central white area shows the characteristics of the platform.

rectangular distribution. For a more direct comparison, the longitudinal profiles of both distributions are extracted, considering identical shape dimensions $L_s = 142m$ (Lindenmuth et al. (1991)). The result is shown in Fig. 3. For the same hull dimensions, the hyperbolic tangent pressure distribution is wider than the Gaussian pressure distribution, even when its peak value approaches the lower bound ($\alpha_{xs} = 6$) required to remain near unity. In fact, it is slightly broader overall than the Gaussian distribution with an exponent factor of $n_x = 8$. This implies a larger displaced volume and consequently a stronger disturbance to the free surface.

Furthermore, as α_{xs} increases, the shape of the hyperbolic tangent pressure distribution gradually approaches a rectangle. It can also be observed that the curves corresponding to different α_{xs} values intersect near the half-peak height, which corresponds to the half-length of the hull. To quantify this width, it is necessary to determine the horizontal coordinate value x corresponding to a given height $S_H(x)$ (i.e., to solve Eq. (18) for x). The expression $2\alpha_x x$ can be solved as follows:

$$2\alpha_x x = \pm \operatorname{arccosh}\left(\frac{\sinh(\alpha_x L_s)}{S_H(x)} - \cosh(\alpha_x L_s)\right) \tag{20}$$

Taking the positive branch and imposing the condition that the shape peak remains close to unity (i.e., $\alpha_{xs} \geq 6$), a further approximation can be made, and Eq. (20) can be rewritten as Eq. (21) and Eq. (22) (proofs for Eqs. (20)–(22) are provided in Appendix A.):

$$2|x| \approx L_s + \frac{1}{\alpha_x}\ln\left(\frac{1 - S_H(x)}{S_H(x)}\right) \tag{21}$$

$$|x| \approx L_s \bigg/ 2\cdot\left(1 + \frac{1}{\alpha_{xs}}\ln\left(\frac{1 - S_H(x)}{S_H(x)}\right)\right) \tag{22}$$

The equations above indicate that the width of the hyperbolic tangent pressure distribution is primarily determined by the characteristic length L_s, with α_{xs} acting as an additional parameter that influences the steepness of the distribution. Larger values of α_{xs} cause the distribution to approach an ideal rectangular shape. When $S_H(x) = 0.5$, one can obtain $|x| \approx L_s/2$, meaning that the full width at half maximum (FWHM) equals the hull length. This precisely reflects the pattern shown in Fig. 3, as described earlier, and the characteristic differs from that of the Gaussian pressure distribution, whose curves for different values of n intersect at the peak level corresponding to $1/a$, as detailed in Bao et al. (2026).

It should be emphasized that the pressure distributions considered in the present study are modeled by finite-sized pressure distributions, rather than by an idealized point-pressure source. For a point source, Ursell (1960), based on the asymptotic analysis of Chester et al. (1957), showed that the wave amplitude along the track may become unbounded because of the contribution of divergent waves. Such behavior is generally regarded as a mathematical singularity associated with the idealized point-source formulation, and the corresponding extremely steep waves are not physically realistic. In contrast, when a finite-sized pressure patch is adopted, the singular behavior is naturally removed (Darmon et al., 2014). In addition, viscous effects have also been shown to suppress such unbounded behavior through wave damping, especially for steep waves (Liang and Chen, 2019). Since the Gaussian, flat-top Gaussian, and hyperbolic-tangent pressure distributions adopted in the present study all have finite spatial extent, the above point-source singularity is not relevant to the present formulations, although viscous damping is not explicitly included.

3. Results and discussion

3.1. The impact of the number of grids in HOS-Ocean

As shown in Fig. 4, in HOS-Ocean (a code based on high order spectral method), the computational domain is a rectangular area with length and width of $xlen_{tot}$ and $ylen_{tot}$ in the x and y directions, respectively. The origin of the coordinate system is located at its lower-left corner, and the z-axis follows the right-hand rule, pointing vertically upward from the plane. No explicit wave-absorption zone was applied in the present HOS-Ocean computations. The simulations were performed in a periodic spectral domain, and boundary effects were reduced by choosing a sufficiently large computational domain. Since the solution is computed via the Fast Fourier Transform (FFT), a uniformly spaced rectangular grid is employed. Let the number of grids in the x and y directions be n_1 and n_2, respectively, and then the maximum resolvable wavenumber $k_{x,max}$ and $k_{y,max}$ are given by Eq. (23):

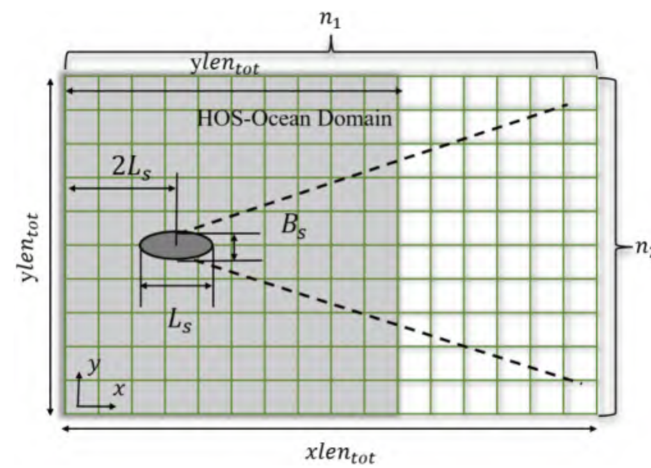

Fig. 4. HOS-Ocean domain mesh configuration (schematic diagram): $xlen_{tot} = xlen \times \lambda_h$ and $ylen_{tot} = ylen \times \lambda_h$, where $xlen$ and $ylen$ are integers, $\lambda_h = gTp_{real}^2/(2\pi)$ is the wavelength, which is determined based on the input significant wave period Tp_{real}. The shaded area in Fig. 4 represents a square region to extract the free-surface elevation data and calculate the power spectral density.

$$k_{x,max} = \frac{2\pi n_1}{xlen_{tot}}, k_{y,max} = \frac{2\pi n_2}{ylen_{tot}} \tag{23}$$

The pressure distribution is positioned at the mid-width of the computational domain and at a distance of twice the ship length $2L_s$ from the left inlet. In HOS-Ocean, to avoid aliasing, the grid is often further refined, for instance by a factor of two. Consequently, within the length and width scale represented by the pressure distribution, the approximate number of grid points n_L and n_B becomes:

$$n_L = \alpha_L \frac{2n_1 L_s}{xlen_{tot}}, n_B = \alpha_B \frac{2n_2 B_s}{ylen_{tot}} \tag{24}$$

where $\alpha_L, \alpha_B > 1$, indicates that the actual range represented by the pressure distribution is slightly broader than the hull itself, and Eq. (24) can written as Eq. (26).

$$\frac{n_L}{n_B} = \frac{\alpha_L}{\alpha_B}\cdot\frac{ylen_{tot}}{xlen_{tot}}\cdot\frac{L_s}{B_s}\cdot\frac{n_1}{n_2} \tag{25}$$

$$\frac{n_L/L_s}{n_B/B_s} = \frac{\alpha_L}{\alpha_B}\cdot\frac{ylen_{tot}}{xlen_{tot}}\cdot\frac{n_1}{n_2} \tag{26}$$

When $\alpha_L = \alpha_B$, given that hull forms are generally slender, ensuring an equal number of grids along the ship length and beam directions imposes a more stringent requirement on the transverse grid count n_2 compared to the longitudinal count n_1. If the objective is instead to maintain an equal grid density per unit length in both directions (i.e. square grid cells, as Eq. (26)), this constraint is relatively relaxed; however, this could result in inaccurate computational results due to distorted pressure distribution, particularly in the transverse direction.

As shown in Fig. 4, a uniform incoming flow is considered to simulate the motion of the pressure distribution, with a flow velocity of U aligned

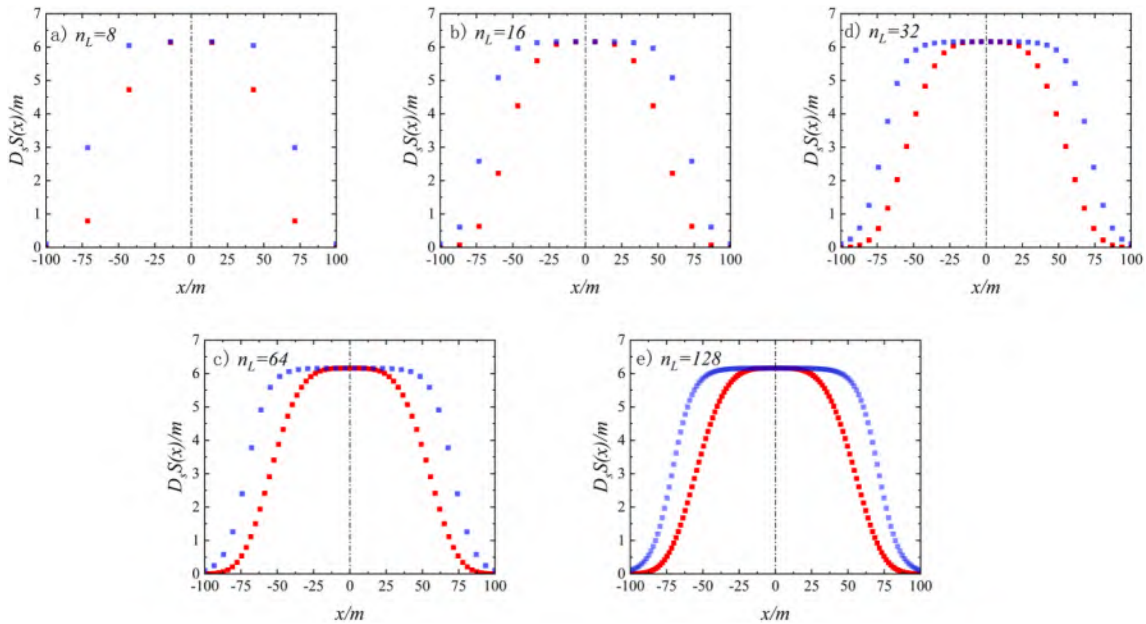

Fig. 5. The longitudinal profiles of pressure distributions corresponding to different grid point numbers. Red points: Gaussian pressure distribution represented by Eq. (15), with parameters $n_x = n_y = 4$ and $\alpha_x = \alpha_y = 7.39$; Blue points: hyperbolic tangent pressure distribution represented by Eq. (18), with parameters $\alpha_{xs} = 10$. Subfigures a) to e) correspond to the grid point numbers $n_1 = 64, 128, 256, 512, 1024$, respectively. (For interpretation of the references to color in this figure legend, the reader is referred to the Web version of this article.)

with the positive x-direction. This corresponds to a rectilinear motion of the pressure distribution along the x-axis, which generates a Kelvin wake system within the wedge-shaped region behind it. Taking the deep-water condition as an example, the dispersion relation of the wave system in the absence of viscous effects is given by:

$$k_y^2 = k_x^2\left(\frac{U^4}{g^2}k_x^2 - 1\right) \tag{27}$$

where k_x and k_y represent the wave number in x and y directions, respectively. Setting $k_y = 0$ yields the cutoff wavenumber $k_x^c = g/U^2$, representing the minimum k_x required for ship wave formation. Therefore, to enable the generation of a Kelvin wake system in HOS-Ocean, the maximum resolvable wavenumber must at least exceed the cutoff wavenumber k_x^c, expressed as Eq. (28):

$$k_{x,max} = \alpha_k \cdot k_x^c, \alpha_k \geq 1 \tag{28}$$

where α_k is a proportionality coefficient. A larger value indicates a greater number of wave number components in the Kelvin wake system, which increases the number of grids required in the computational domain. From this perspective, the minimum number of grid points $n_{1,min}$ required to generate the Kelvin wake system is given by:

$$n_{1,min} = \alpha_k \frac{g}{2\pi U^2} \cdot xlen_{tot} \tag{29}$$

Consider the DTMB5415 hull, the ship length L_s, beam B_s, and draft D_s are 142 m, 18.9 m, and 6.16 m, respectively, with a water depth h of 171 m (corresponding to deep-water condition). Assuming $Tp_{real} = 10$ s and setting *xlen* and *ylen* to 20 and 10, respectively, the computational domain size in HOS-Ocean is 3120m × 1560 m. Taking a Froude number of $Fr = U/\sqrt{gL_s} = 0.414$ (corresponding to $U = 15.452\ m/s$) and setting $\alpha_k = 3$ (a relatively small number), the minimum number of grids is calculated as $n_{1,min} \approx 62$. This indicates that, for the given computational domain, a minimum of approximately 62 grids in the primary direction is required to generate the Kelvin wake system. With $n_1 = 256$, the number of grid points n_L representing the pressure distribution in the longitudinal direction is approximately 32 (if $\alpha_L = 1.4$, corresponding to the range $\pm 100m$). The longitudinal profiles of the two different distributions of different numbers of scatter points are shown in Fig. 5. And the y-direction is similar.

It is evident that even when the minimum grid requirement for generating the Kelvin wake is satisfied, the fidelity in capturing the pressure distribution's features declines as grid resolution is reduced. This degradation can eventually impede the successful formation of the Kelvin wake. In light of this, taking the Gaussian pressure distribution as an instance, with a total simulation duration set to $T_{stop} = 30 \times Tp_{real}$, the Kelvin wake patterns corresponding to different grid settings were simulated. In the present work, the water depth is assumed to be infinite, so that the analysis is limited to deep-water ship waves. We note, however, that finite-water-depth effects introduce an additional controlling parameter, namely the depth Froude number $F_h = U/\sqrt{gh}$, which can significantly alter the dispersion relation and the resulting wake pattern (Bao et al., 2025; Noblesse and Yang, 2007; Yao et al., 2023; Zhu et al., 2015, 2018). These effects are not considered here and deserve separate investigation.

3.1.1. *Maintain the same grid density in both the longitudinal and transverse directions*

In the current setup, the grid configuration follows the proportional relationship $n_1/n_2 = xlen_{tot}/ylen_{tot}$ to maintain square grid cells, as Eq. (26). The results are presented as Fig. 6. When the grid resolution is low (e.g., $n_1 = 64$), the simulated Kelvin wake mainly consists of transverse waves, with divergent waves being scarcely visible. This limitation arises because the maximum representable wavenumber $k_{x,max}$ is insufficient to capture the broader spectral content of the wake. As the grid number increases, divergent waves become distinctly apparent in the wake pattern. This occurs because a finer grid supports a higher maximum wavenumber $k_{x,max}$, allowing the shorter wavelengths characteristic of divergent waves to be resolved—confirming that divergent waves correspond to larger wavenumbers than transverse waves. Improved grid resolution also enhances the clarity and detail of the free surface contour. At $n_1 = 256$, the results closely match those obtained

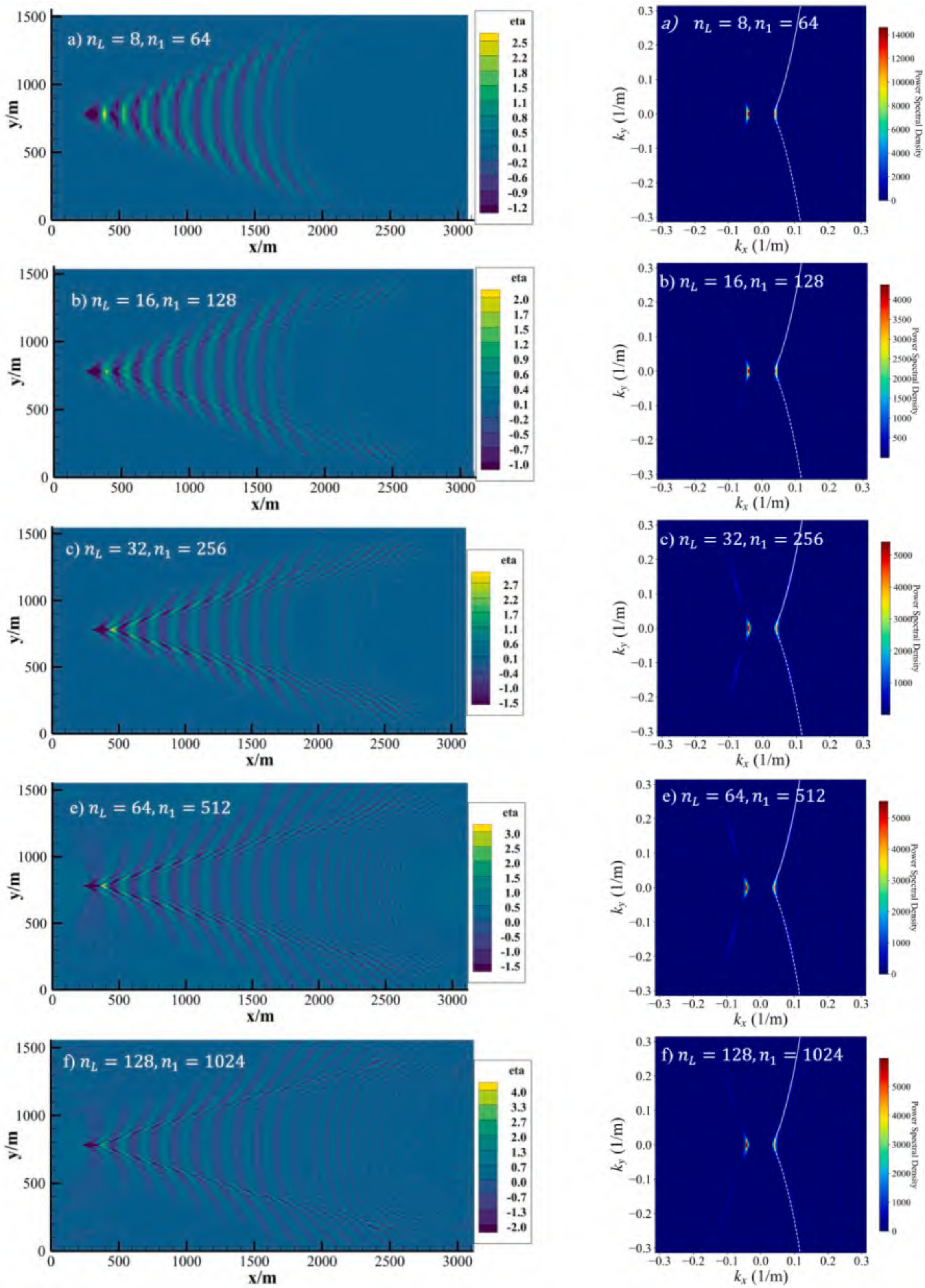

Fig. 6. Results of Gaussian pressure distribution under different grid configurations: $n_1 = 64, 128, 256, 512, 1024, n_2 = 0.5n_1$. Left column: Kelvin wake patterns; Right column: power spectral density, and the white line represents the theoretical dispersion curve expressed by Eq. (27).

with even finer grids, indicating that the solution has nearly converged for this configuration.

As illustrated in Fig. 4, the power spectral density (PSD) is computed from the free surface elevation data within a square region whose side length equals the width of the computational domain (i.e. $ylen_{tot}$) and whose origin is placed at the lower-left corner. The resulting spectrum is presented in Fig. 6 (right column). It should be noted that the correspondence between the wave pattern in physical space and the dispersion curve in Fourier space has been well established in the literature. In particular, Lighthill (1978) provided a systematic interpretation of this relationship, and related extensions have been reported for capillary-gravity ship waves and time-harmonic ship waves by Liang and Chen (1999, 2018), respectively. In the present study, the 2D FFT result is used mainly to confirm that the dominant wavenumber components of the numerically generated wake are consistent with the classical dispersion characteristics of steady ship waves.

Consistent with the trends observed in Fig. 6, when the grid resolution is low (e.g., $n_1 = 64$), the power spectral density is prominent only near the cutoff wavenumber k_x^c, which corresponds to transverse waves with relatively small wavenumbers. As the number of grids increases, the power spectrum exhibits a distinct X-shaped arm pattern, corresponding to divergent waves that possess higher wavenumbers than transverse waves. With further grid refinement, the extension range of the X-shaped arms expands, reflecting that the increased maximum resolvable wavenumber $k_{x,max}$ at higher resolution enables the representation of richer spectral components of the wake system. When $n_1 = 1024$, a slight deviation emerges between the two spectral arms and the theoretical dispersion curve. The underlying reason lies in the core of the pseudo-spectral method—the Fast Fourier Transform (FFT). To ensure numerical stability and prevent divergence, high-frequency noise must be filtered out during computation. When the grid number becomes excessively large, insufficient filtering may occur, leading to numerical oscillations and the introduction of high-frequency noise. This issue is evident in the free surface elevation data (i.e. η) extracted at a distance of 46 m from the pressure center ($y' = 46$ m), as shown in Fig. 7 (e.g. subfigure e)), where the curve exhibits unsmooth, noisy fluctuations.

It should be noted that these simulations were performed on a 3.60 GHz Intel Core i7-9700 single-core processor; therefore, insufficient computational power could also be a contributing factor. However, for this specific case configuration, the actual runtime was only about 10 min for $n_1 = 256$ and merely a few seconds for $n_1 = 64$, suggesting that raw processing capability may not be the primary bottleneck in this instance. However, more in-depth comparative analysis is still required (which could involve the use of more powerful computational resources).

When the number of grids is too small, the computational results can lose accuracy, while an excessively fine grid may introduce high-frequency noise. For $n_1 = 256, 512$, the simulated wave profiles exhibit close agreement. These results are then compared with the experimental measurements from Lindenmuth et al. (1991), as presented in Fig. 8. It shows a high level of agreement with the experimental

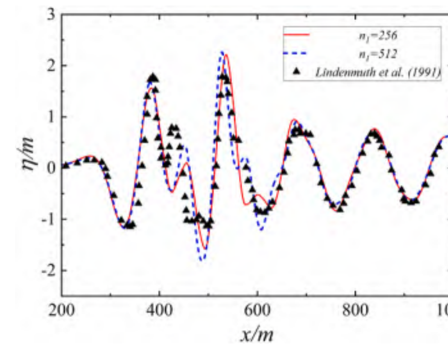

Fig. 8. A comparison of the results for wave surface elevation for two grid sizes with the experiments of Lindenmuth et al. (1991).

values, which further demonstrates that an appropriate number of grid points can effectively characterize the shape features of the pressure distribution while also adequately capturing accurate wavefront information.

3.1.2. The effects of the number of grids n_2 in the y-direction

When the grid density per unit length is identical in both longitudinal and transverse directions, a configuration with $n_1 = 256$ and $n_2 = 128$ appears to yield acceptable result. However, it is noteworthy that under this setup the representation of the pressure distribution in the beam direction appears relatively coarse. Hence, it is necessary to further investigate the influence of the grid resolution in the y-direction. Keeping n_1 fixed at 256 and varying n_2, the Kelvin wake systems corresponding to several different grid configurations were computed, and the results are presented in Fig. 9. Compared with the results shown in Fig. 6, both the free-surface contours and the power spectral densities exhibit minimal variation, and the observed trends remain consistent. As the grid resolution increases, the structure of the wave system becomes progressively clearer, and a greater portion of the divergent-wave components is captured.

Similarly, the free-surface elevation data was extracted at a distance of 46 m from the pressure center plane and compared with experimental measurements (Lindenmuth et al. (1991)). As shown in Fig. 10, for $n_2 = 128, 256, 512$, the results appear to have reached an acceptable level of accuracy. This indicates that for the Gaussian pressure distribution used,

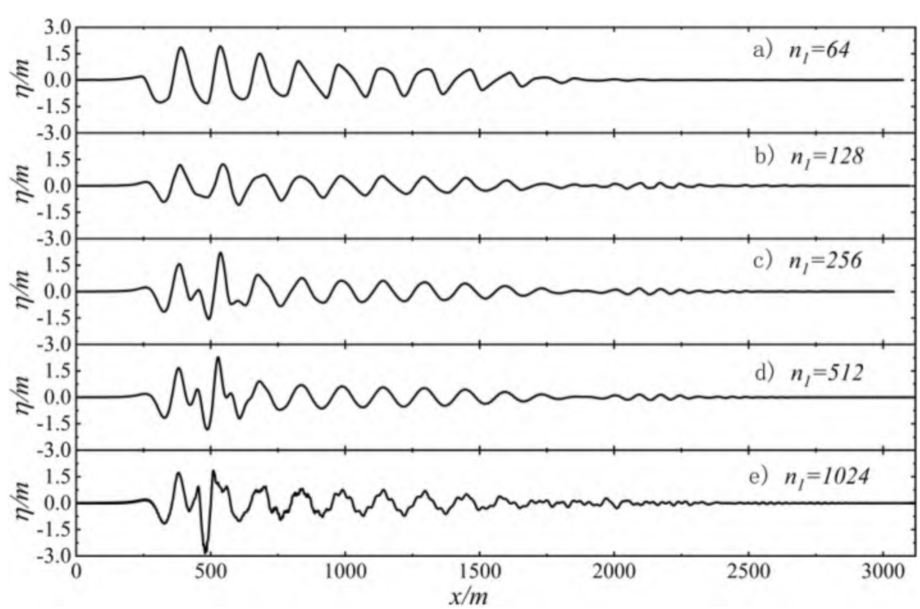

Fig. 7. Free surface elevation data at a distance of 46m from the pressure centre ($y' = 46m$) for wave systems with different grid numbers.

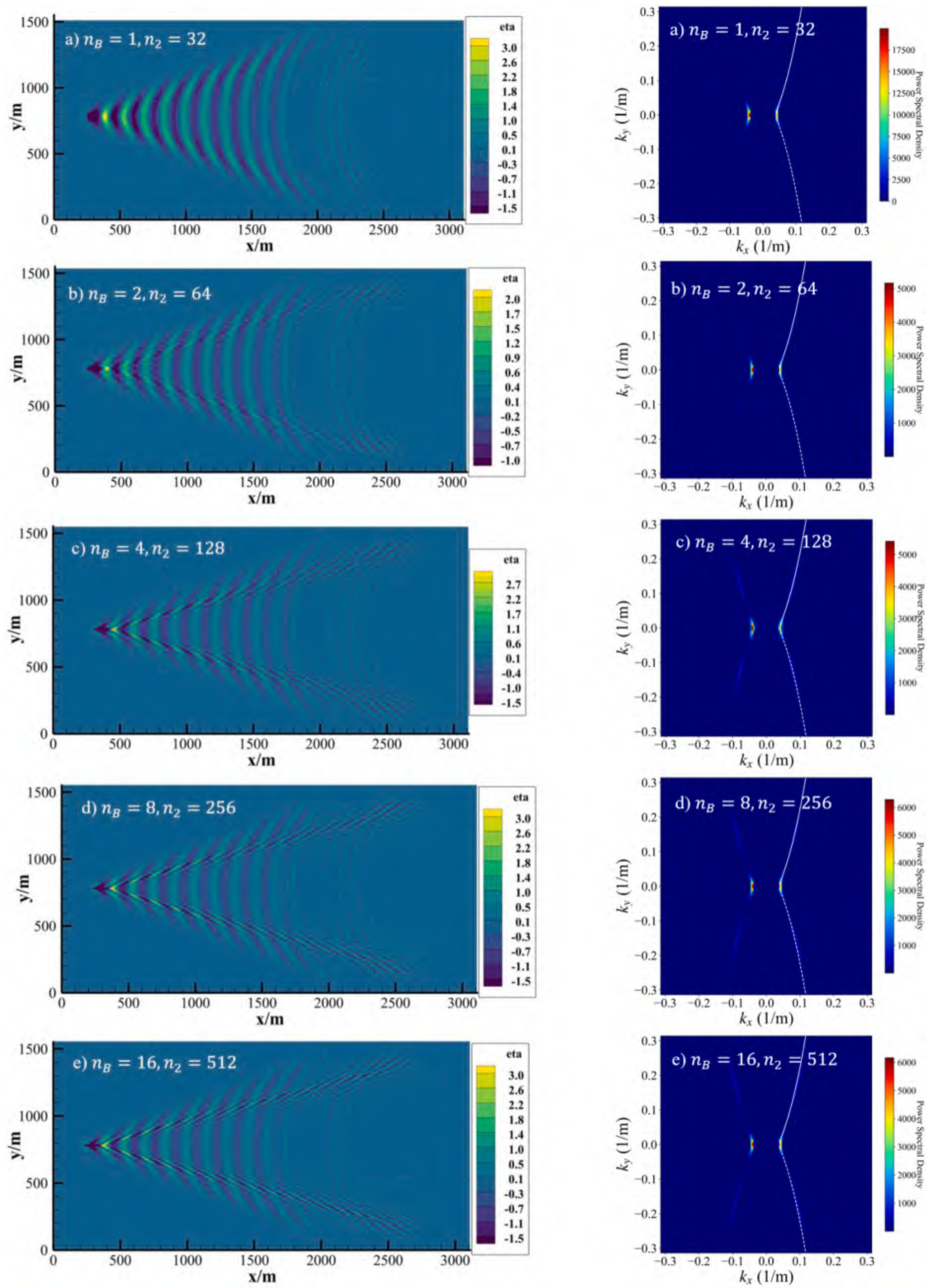

Fig. 9. Results of Gaussian pressure distribution under different grid configurations: $n_1 = 256, n_2 = 32, 64, 128, 256, 512$. Left column: Kelvin wake patterns; Right column: power spectral density, and the white line represents the theoretical dispersion curve expressed by Eq. (27).

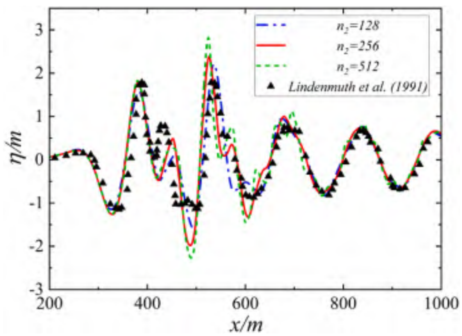

Fig. 10. A comparison of the results for wave surface elevation for three grid sizes with the experiments of Lindenmuth et al. (1991).

approximately 10 grid points across the hull width and 32 grid points along the hull length are sufficient to adequately represent the pressure distribution and thereby compute a reasonably accurate Kelvin wake system. For flatter distributions, the required number of grids can be appropriately reduced, as is the case with the standard Gaussian pressure distribution. Certainly, increasing the grid resolution appropriately should, in principle, improve the representation of the pressure distribution and lead to more accurate computational results.

It should be noted that when n_2 is increased further, for instance, to $n_2 = 1024$, the computation tends to diverge, and this instability occurs earlier than in the case of $n_1 = 1024$. The reason lies in the higher maximum resolvable wavenumber $k_{y,max}$ associated with a finer transverse grid, which leads to more inadequate filtering in HOS-Ocean and consequently exacerbates numerical oscillations. Improving the filtering algorithm in HOS-Ocean may be necessary to mitigate this effect, though it is not the primary focus of the present study and could be systematically addressed in future work. Consequently, the computational capability of HOS-Ocean is also challenged—at least for the 3.60 GHz Intel Core i7-9700 single-core processor employed here, the upper limit of resolvable wavenumbers appears to be around 4. Therefore, when employing HOS-Ocean to simulate Kelvin wake systems, it is essential to appropriately balance the size of the computational domain with the spatial extent of the pressure distribution representing the hull region. This consideration is crucial both for computational efficiency and for ensuring the accuracy of the results.

3.2. Power spectral density of the Kelvin wake in different selected regions

The free-surface elevation data extracted from the shaded region indicated in Fig. 4 does not encompass the entire simulated Kelvin wake system. Consequently, whether the power spectral density (PSD) derived from such a sub-region can adequately represent the spectral characteristics of the full wake remains to be verified. In this study, we therefore preliminarily adopt two complementary evaluation approaches to compare the PSD computed from different selected sub-regions.

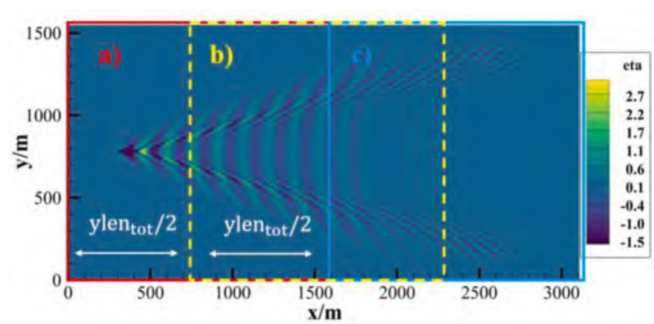

Fig. 11. Scheme 1: Three equal-sized square regions, each with a side length equal to the computational domain width, spaced at half-width intervals (i.e. $ylen_{tot}/2$).

The first selection scheme is illustrated in Fig. 11, where three square sub-regions (a, b, c) are chosen, each with a side length equal to the width of the computational domain (i.e. $ylen_{tot}$). These squares are spaced at intervals of $ylen_{tot}/2$. Taking $n_1 = 256, n_2 = 128$ as an example (e.g. Fig. 6 or Fig. 9 c)), the PSD calculated for these three regions are presented in Fig. 12. The PSD of all sub-regions exhibit an X-shaped pattern, with overall differences being minimal. Each aligns well with the corresponding theoretical dispersion relation curve. As the waves propagate downstream and their heights diminish, the spectral magnitudes decrease. To some extent, the PSD of sub-region a) can already adequately represent the overall spectral characteristics of the wake system.

Although the PSDs extracted from the three selected sub-regions show some differences in magnitude, their dominant structures remain highly consistent, since all of them exhibit the characteristic X-shaped pattern and agree well with the theoretical dispersion relation. The main difference is observed in sub-region c), where the transverse-wave peaks become weaker, the divergent-wave branches appear relatively more pronounced, and the spectral distribution near the central region becomes more sparse. Since sub-region c) is located farther downstream, the free-surface elevation has decayed more significantly, leading to a lower overall PSD level. In addition, wave trains generated from different points of the pressure distribution undergo destructive interference, leading to the fragmentation of transverse waves. At greater distances, even when constructive interference occurs, transverse waves remain less distinct due to wave-amplitude attenuation. As a result, the divergent-wave branches become relatively more visible in the PSD. Nevertheless, the dominant X-shaped spectral structure and its agreement with the theoretical dispersion relation remain unchanged, indicating that the underlying Kelvin-wake spectral framework is still well preserved.

As illustrated in Fig. 13, several square sub-regions of varying side lengths are defined, with the midpoint of their left edge aligned with the center of the computational domain's left inlet. Taking the square computational domain with $n_1 = n_2 = 256$ as an example, the corresponding PSD for these different sub-regions are shown in Fig. 14. The PSD corresponding to the three selected regions show hardly differences, indicating that the PSD derived from region a) serves as a reasonable spectral signature of the overall Kelvin wake characteristics.

3.3. The influence of draft selection on pressure distribution

According to Eq. (12), ensuring that the displaced volume of the actual ship equals that represented by the pressure distribution hinges on the spatial integral I of the shape function $S(x,y)$. For ease of discussion, the integration limits are here taken as infinite in both directions.

$$I = \int_{-\infty}^{+\infty} \int_{-\infty}^{+\infty} S(x,y)\mathrm{d}x\mathrm{d}y \tag{30}$$

For the Gaussian and hyperbolic tangent pressure distributions considered in this study, the shape functions in the x and y-directions share the same mathematical form, implying that $S(x,y) = S(x)\cdot S(y)$ holds. Therefore, one can have:

$$I = \int_{-\infty}^{+\infty} S(x)\mathrm{d}x\cdot \int_{-\infty}^{+\infty} S(y)\mathrm{d}y = I_x\cdot I_y \tag{31}$$

where I_x and I_y are spatial integral in x and y directions respectively. Proofs for Eqs. (32) and (36) are provided in Appendix B.

For the Gaussian pressure distribution expressed in Eq. (15), its spatial integral I_{G3} is given by:

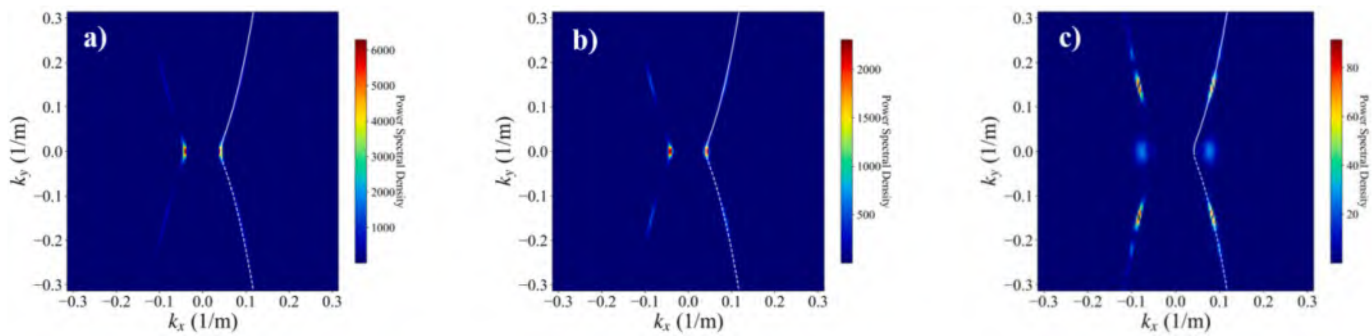

Fig. 12. Power spectrum density in different regions for scheme 1: the white line represents the theoretical dispersion curve expressed by Eq. (27).

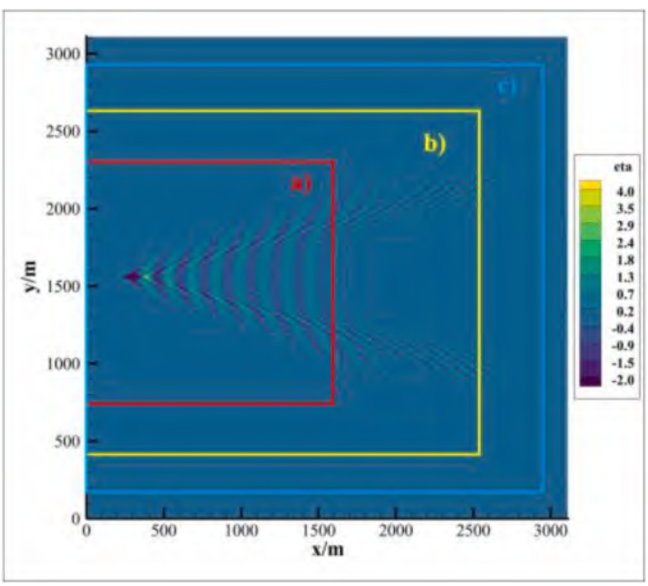

Fig. 13. Scheme 2: Three square regions with different side lengths: a) 1560m, b) 2340m, c) 2730m), with the midpoint of their left edge aligned with the centre of the computational domain's left inlet.

$$I_{G3} = \frac{4L_sB_s}{\beta_x^{1/n_x}\beta_y^{1/n_y}} \cdot \Gamma\left(1+\frac{1}{n_x}\right)\Gamma\left(1+\frac{1}{n_y}\right) \tag{32}$$

and $\beta = 2^n \ln(a)$, then:

$$I_{G3} = \frac{L_sB_s}{(\ln(a_x))^{1/n_x}(\ln(a_y))^{1/n_y}} \cdot \Gamma\left(1+\frac{1}{n_x}\right)\Gamma\left(1+\frac{1}{n_y}\right) \tag{33}$$

where $\Gamma(\xi) = \int_0^{+\infty} x^{\xi-1}e^{-x}dx, \xi > 0$ is the Gamma function, ξ could be $1+\frac{1}{n_x}$ or $1+\frac{1}{n_y}$. In this paper, let $n_x = n_y = n$ and $a_x = a_y = a$, then Eq. (33) can be written as:

$$I_{G3} = \frac{L_sB_s}{(\ln(a))^{2/n}} \cdot \Gamma^2\left(1+\frac{1}{n}\right) \tag{34}$$

The draft D_{sG} for Gaussian pressure distribution can be expressed as:

$$D_{sG} = \frac{m}{\rho} \cdot \frac{(\ln(a))^{2/n}}{L_sB_s \cdot \Gamma^2(1+1/n)} \tag{35}$$

The corresponding values of the Gamma function Γ for several different values of n are provided in Table 2. When $n = 2$, this corresponds to the standard Gaussian pressure distribution (i.e. Eq. (13), and $I = L_sB_s\pi/8$ for $a = 7.39$); as n tends to infinity, the represented volume approaches that of a rectangular domain (i.e. $I_{G3} = L_sB_s$). As the value of n increases, the pressure distribution gradually widens, resulting in a larger displaced volume represented by the distribution. Consequently, for the same displacement mass, the draft D_{sG} decreases. Of course, the value of D_{sG} is also related to a. The larger a is, the larger D_{sG} will be.

Similarly, for the hyperbolic tangent pressure distribution described by Eq. (17), its spatial integral is given by:

$$I_{H2} = L_sB_s \tag{36}$$

It can be observed that the final result of the integral is entirely independent of the steepness parameters α_x and α_y. Regardless of how

Table 2
Special values of the Gamma function Γ for different n values.

n	$\Gamma(1+1/n)$	$\Gamma^2(1+1/n)$
2	$\sqrt{\pi}/2$	$\pi/4$
4	0.9064	0.8216
6	0.9277	0.8607
8	0.9417	0.8869
10	0.9514	0.9061
$+\infty$	1	1

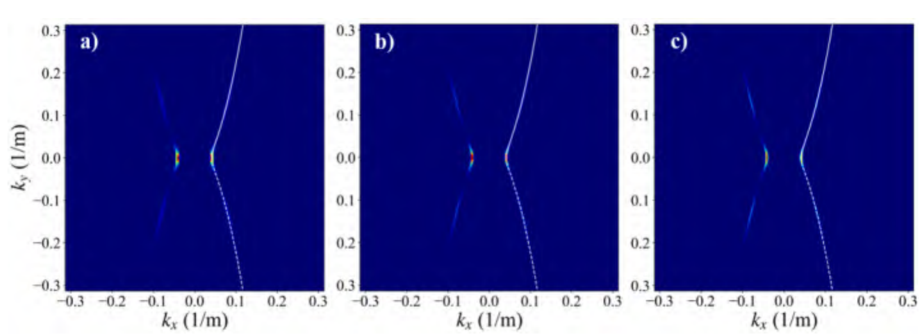

Fig. 14. Power spectrum density in different regions for scheme 2: the white line represents the theoretical dispersion curve expressed by Eq. (27).

sharply or gently the edges are defined, as long as the integration limits extend to infinity, the volume represented by this distribution function remains equal to the product of the effective length L_s and the effective width B_s. When α_x and α_y tend to infinity, the distribution approaches a rectangular shape.

The draft D_{sH} for hyperbolic tangent pressure distribution can be expressed as:

$$D_{sH} = \frac{m}{\rho} \cdot \frac{1}{L_s B_s} \tag{37}$$

D_{sH} is not affected by changes in α_x and α_y, but depends solely on the hull parameters. When the target hull parameters are fixed, the draft corresponding to this distribution remains constant. From this perspective, for the same hull dimensions L_s and B_s, the draft corresponding to the hyperbolic tangent pressure distribution is smaller than that of the Gaussian pressure distribution.

The block coefficients for the two pressure distributions are calculated as follows:

Gaussian pressure distribution:

$$C_{bG} = \frac{\Gamma^2(1 + 1/n)}{(\ln(a))^{2/n}} \tag{38}$$

Hyperbolic tangent pressure distribution:

$$C_{bH} = 1 \tag{39}$$

The block coefficient of the hyperbolic tangent pressure distribution is exactly 1, indicating that it may be more suitable for modelling full-formed hulls. In contrast, the block coefficient of the Gaussian pressure distribution can vary continuously, which allows it to represent a wider range of hull forms, from slender to relatively full vessels.

As mentioned earlier, consider the DTMB5415 hull, the ship length L_s, beam B_s, and draft D_s are 142 m, 18.9 m, and 6.16 m (real ship), and the displacement volume based on the 6.16m draft to be 8425.4 m^3, respectively. For the Gaussian pressure distribution with $a = 7.39$, when $n = 2$ (referred to as the standard Gaussian pressure distribution in this paper), the block coefficient is $C_{bG} = 0.3927$ and the draft is $D_{sG} = 7.994$ m; when $n = 4$ (referred to as the flat-top Gaussian pressure distribution in this paper), $C_{bG} = 0.5809$ and $D_{sG} = 5.4039$ m. For the hyperbolic tangent pressure distribution, the draft is $D_{sH} = 3.1393$ m. The computational domain size in HOS-Ocean is set as 3120m × 1560 m, and a total simulation duration set to $T_{stop} = 300$ s, and $Fr = 0.414$. Let $n_1 = 256$ and $n_2 = 256$, which means n_L and n_B approximately are 32 and 8, respectively.

The longitudinal profiles of the two different distributions of different draft are shown in Fig. 15. The standard Gaussian pressure distribution exhibits a concentrated profile with minimal lateral "shoulders," resulting in the largest draft for a given displaced mass *m*. In contrast, the flat-top Gaussian distribution displays more defined shoulders as pressure extends from the center toward the sides, corresponding to a moderately reduced draft. The hyperbolic tangent distribution presents an even broader profile, with the smallest draft among the three. While these pressure distributions differ in draft, the spatial extents they represent remain broadly similar. However, when constrained to an identical draft value, their represented areas diverge noticeably, as shown in Fig. 5. Mathematically, D_s acts as a scaling coefficient applied to a normalized shape function with a peak value of unity. Increasing D_s steepens the flanks of the pressure distribution—a behavior that differs from actual hull geometry, where draft variation does not alter the hull form. Nevertheless, this approach offers a reasonable approximation for modeling purposes.

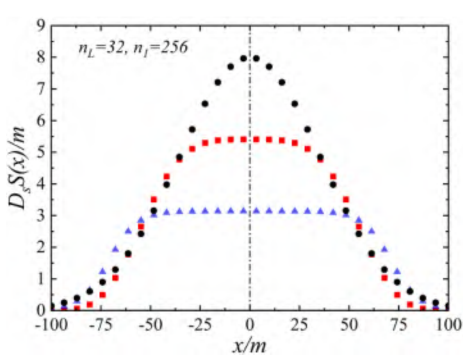

Fig. 15. Longitudinal profiles under different pressure distributions at the same displacement. Black circle: Gaussian pressure distribution within $a = 7.39$, $n = 2$ and $D_{sG} = 7.994$ m; Red block: Gaussian pressure distribution within $a = 7.39$, $n = 4$ and $D_{sG} = 5.4039$ m; Blue triangle: hyperbolic pressure distribution within $\alpha_{xs} = 10$ and $D_{sH} = 3.1393$ m. (For interpretation of the references to color in this figure legend, the reader is referred to the Web version of this article.)

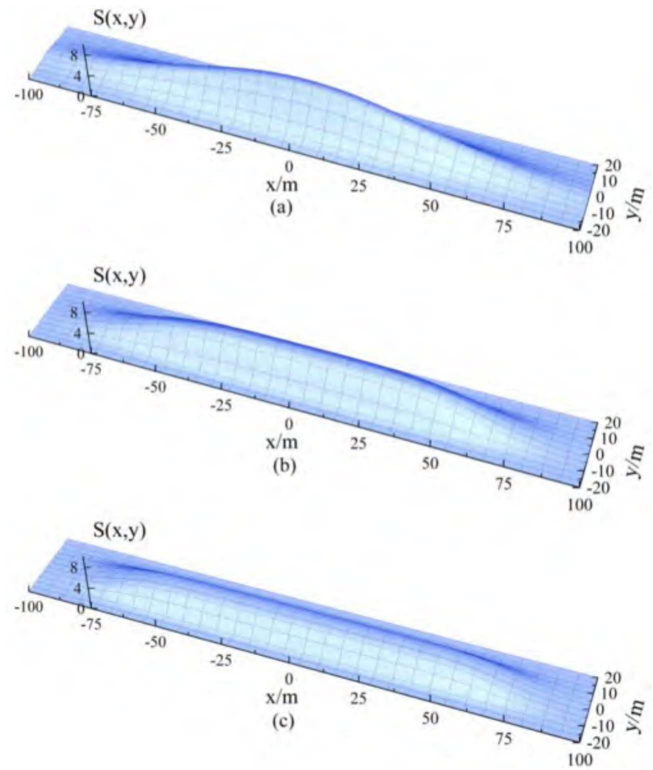

Fig. 16. Three-dimensional view of different pressure distributions under equal drainage quality. (a): standard Gaussian pressure distribution within $a = 7.39$, $n = 2$ and $D_{sG} = 7.994$ m; (b): flat-top Gaussian pressure distribution within $a = 7.39$, $n = 4$ and $D_{sG} = 5.4039$ m; (c): hyperbolic pressure distribution within $\alpha_{xs} = 10$ and $D_{sH} = 3.1393$ m.

The three-dimensional representations of these three pressure distributions are shown in Fig. 16. Although the number of grids used is relatively limited, the fundamental characteristics of the distributions are already clearly represented owing to their favorable mathematical properties.

The Kelvin wake systems were computed for these scenarios (three pressure distributions under two different drafts), considering the actual hull draft ($D_s = 6.16m$) for the pressure distribution, and results are shown in Fig. 17. It should be noted that for the same pressure distribution, variations in draft (where the draft obtained from integration differs only slightly from the actual draft) result in wave-field contours and power spectral densities that are very similar in overall shape, with the main difference being the amplitude. Therefore, for conciseness, only the results comparing different pressure distributions under different drafts are presented here.

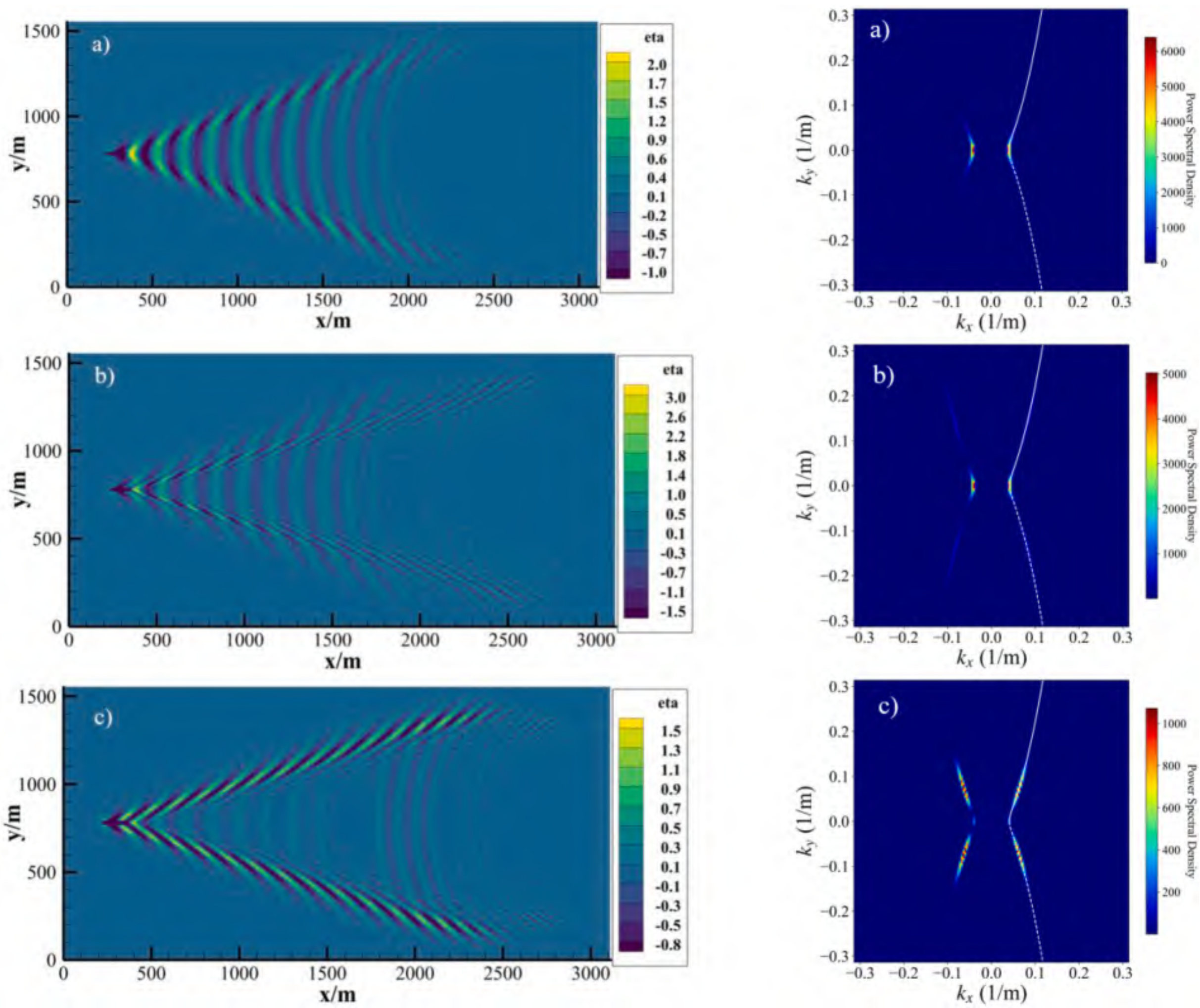

Fig. 17. Results of different pressure distributions under equal drainage quality: Left column: Kelvin wake patterns; Right column: power spectral density, and the white line represents the theoretical dispersion curve expressed by Eq. (27). And (a): standard Gaussian pressure distribution within $a = 7.39$, $n = 2$ and $D_{sG} = 7.994$ m; (b): flat-top Gaussian pressure distribution within $a = 7.39$, $n = 4$ and $D_{sG} = 5.4039$ m; (c): hyperbolic pressure distribution within $\alpha_{xs} = 10$ and $D_{sH} = 3.1393$ m.

Compared to the standard Gaussian pressure distribution, the flat-top Gaussian distribution generates a more pronounced bow wave system with richer divergent-wave components. Overall, however, both distributions produce clearly identifiable transverse and divergent waves. In contrast, the Kelvin wake produced by the hyperbolic tangent pressure distribution is dominated by divergent waves, while the transverse waves appear to undergo more significant destructive interference, resulting in a more fragmented pattern. Correspondingly, the power spectral density exhibits more prominent X-shaped arms associated with the divergent waves, whereas the spectral content near the cutoff wavenumber k_x^c is nearly absent. This difference arises from the distinct spatial extents represented by the three distributions, which naturally leads to variations in the interference patterns of the wave systems.

As shown in Fig. 18, a larger draft generates a wake system with higher free-surface elevation. When the drafts are relatively close, the differences in free-surface elevation are minor (e.g., Fig. 18(a) and (b)). Because the hyperbolic tangent pressure distribution has a larger block coefficient (and thus a larger displaced volume), its derived draft deviates more substantially from the actual draft, leading to a more pronounced discrepancy in the resulting free-surface elevation. This suggests that the Gaussian pressure distribution is less sensitive to the choice of draft—at least when the exponent n is selected within a similar range, the resulting wave patterns remain comparable. Under these conditions, both the draft determined from mass-equivalence and the actual draft yield reasonably acceptable results. Furthermore, compared with the Gaussian distribution, the free-surface elevation curve produced by the hyperbolic tangent distribution shows a markedly different trend and a clear phase shift relative to the experimental data. This discrepancy arises from the broader shape of the distribution, which modifies the mutual interference of the generated waves. This also indicates that the hyperbolic tangent pressure distribution is less suitable for representing the hull form considered in this study.

3.4. Kelvin wake at different Froude numbers Fr_L

Here, the Froude number based on ship length L_s, denoted as Fr_L, is defined (i.e. $Fr_L = U/\sqrt{gL_s}$, where U is velocity). Following the computational configurations described in Section 3.3, the Kelvin wake systems corresponding to the two different pressure distributions (i.e. flat-top Gaussian pressure distribution and hyperbolic pressure distribution) are calculated at several Froude numbers (all lower than the value 0.414 used earlier). To ensure an equivalent disturbance on the free-surface, the draft is determined by matching the displaced mass. The Kelvin wake generated by the standard Gaussian pressure distribution is not computed (its results can be referred to in Bao et al. (2025)); only the wave systems corresponding to two broader pressure

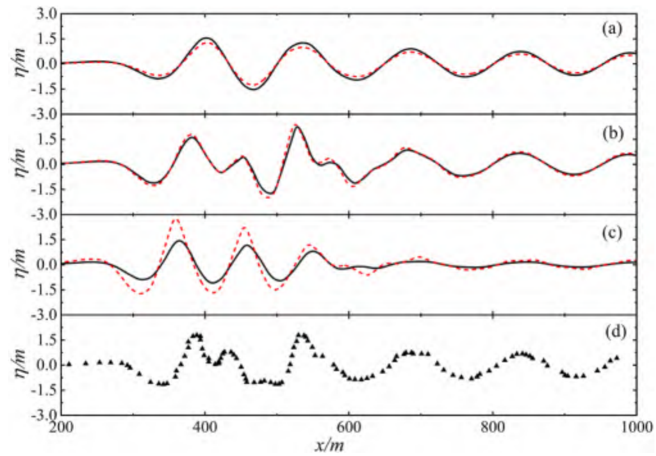

Fig. 18. Free surface elevation data at a distance of 46m from the pressure centre ($y' = 46m$) for wave systems with different pressure distributions. Solid black lines: (a): standard Gaussian pressure distribution within $a = 7.39$, $n = 2$ and $D_{sG} = 7.994$ m; (b): flat-top Gaussian pressure distribution within $a = 7.39$, $n = 4$ and $D_{sG} = 5.4039$ m; (c): hyperbolic pressure distribution within $\alpha_{xs} = 10$ and $D_{sH} = 3.1393$ m; Red dashed lines: real ship draft, $D_s = 6.16m$ for the three pressure distributions; (d): experimental measurements (Lindenmuth et al. (1991)). (For interpretation of the references to color in this figure legend, the reader is referred to the Web version of this article.)

distributions are calculated. The results are presented in Figs. 19 and 20, respectively.

Firstly, each of the two pressure distributions generates its own distinct Kelvin wake system, and the X-shaped arms in their power spectral densities align well with the theoretical dispersion relation curves. As the Froude number Fr_L gradually decreases, the resulting Kelvin wake becomes progressively less pronounced. When $Fr_L < 0.25$, the flat-top Gaussian pressure distribution appears to lose its ability to produce a clearly visible Kelvin wake. For the standard Gaussian distribution, this threshold is approximately 0.3, whereas for the hyperbolic tangent distribution it is around 0.2. This indicates that the hyperbolic tangent pressure distribution seems to excite wave systems more readily, suggesting that a broader effective area represented by the pressure distribution facilitates wave generation.

Secondly, compared with the standard Gaussian distribution, both the flat-top Gaussian and hyperbolic tangent distributions generate more discernible bow and stern wave systems. This difference stems from the concentrated nature of the standard Gaussian distribution, which lacks pronounced “shoulders” and exhibits smooth ends. Consequently, the transverse waves generated by the standard Gaussian distribution experience minimal destructive interference. In contrast, the flat-top Gaussian and hyperbolic tangent distributions, with their more extended lateral profiles, promote stronger destructive interference, causing the transverse waves in the wake to appear fragmented or intermittent visually. It should be noted that the apparent attenuation of far-field transverse waves in the wave-pattern plots is influenced by the color bar threshold. Due to the destructive interference between the bow

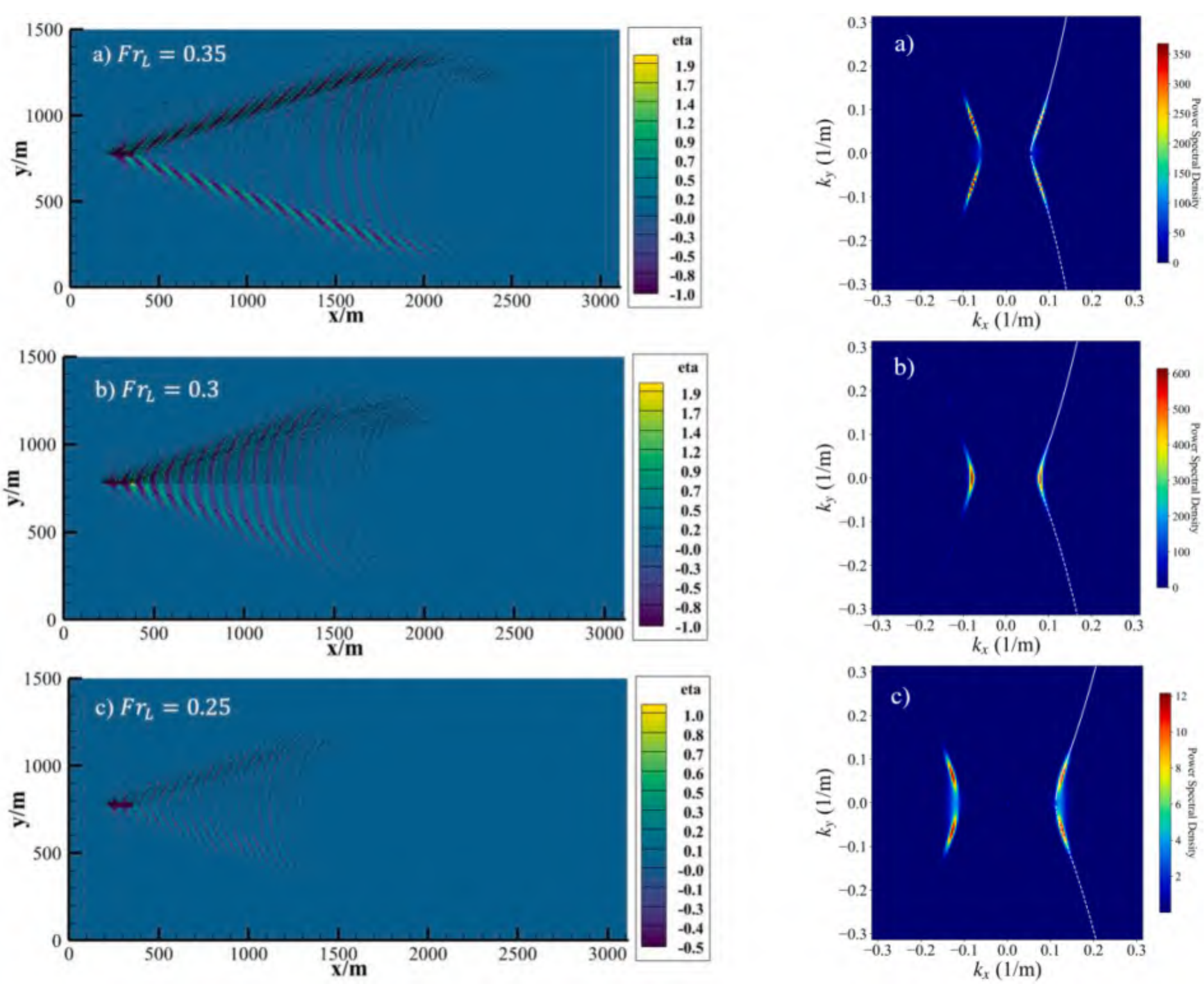

Fig. 19. Results of flat-top Gaussian pressure distribution within $a = 7.39$, $n = 4$ and $D_{sG} = 5.4039$ m at different Fr_L: Left column: Kelvin wake patterns; Right column: power spectral density, and the white line represents the theoretical dispersion curve expressed by Eq. (27).

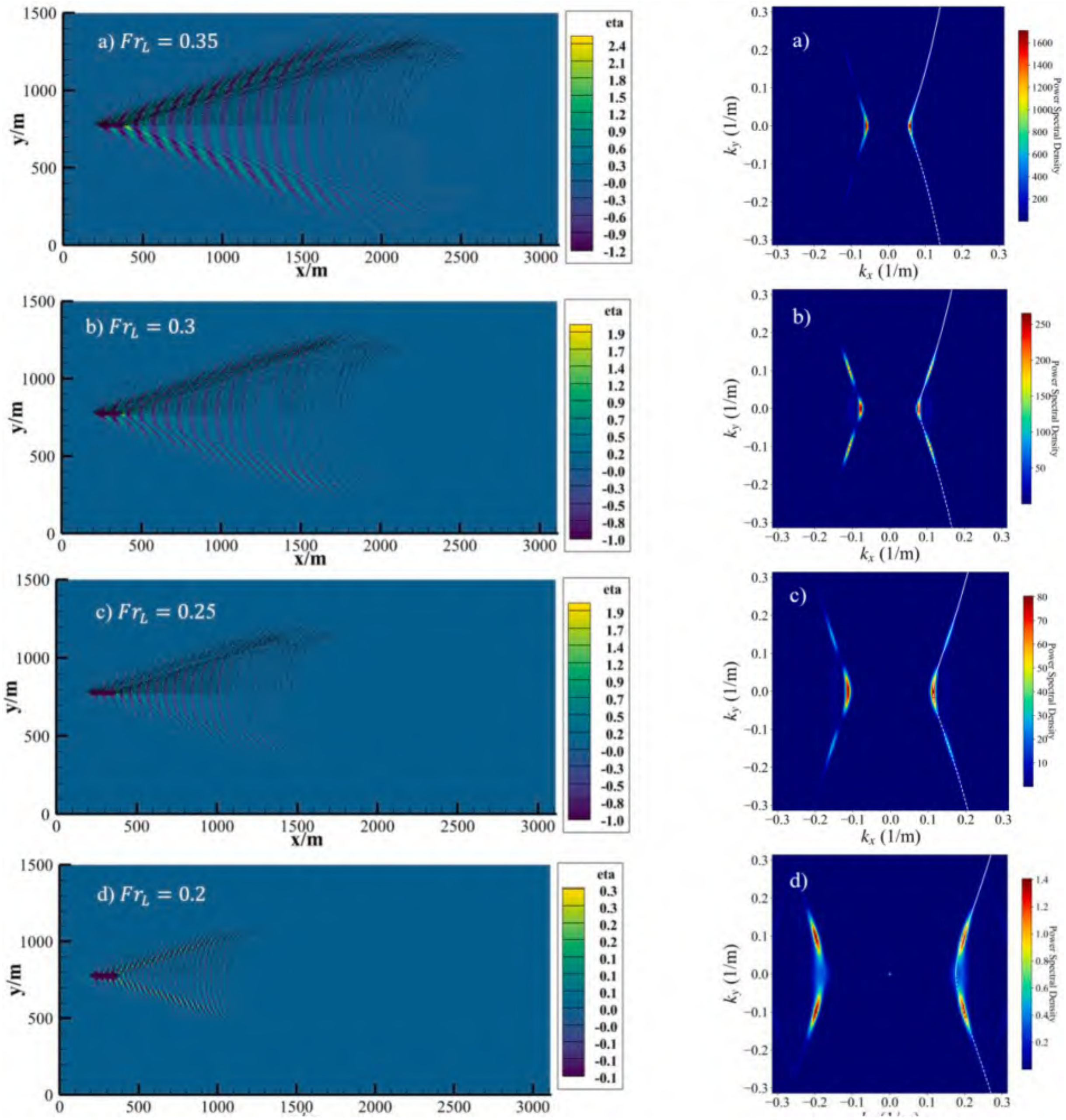

Fig. 20. Results of hyperbolic pressure distribution within $\alpha_{xs} = 10$ and $D_{sH} = 3.1393$ m at different Fr_L: Left column: Kelvin wake patterns; Right column: power spectral density, and the white line represents the theoretical dispersion curve expressed by Eq. (27).

and stern wave systems, the transverse-wave amplitude becomes weak in some regions and may become visually indistinct under an unsuitable plotting range. In addition, the apparent shortening of the far-field transverse wavelength is not regarded as physical. Theoretically, the transverse wavelength should remain nearly constant along a fixed ray angle. The slight irregularity in crest spacing observed in some HOS-Ocean results is more likely related to accumulated phase errors associated with high-wavenumber filtering and dealiasing during long-time propagation, together with visualization effects. This is also supported by the extracted longitudinal wave cut (Fig. 7), which shows no obvious change in the transverse wavelength.

4. Conclusions

In this study, the open-source software HOS-Ocean, based on the high order spectral (HOS) method, is employed to generate and evolve Kelvin wake systems by introducing different pressure distributions into the dynamic free-surface boundary condition, thereby extending the range of applications of HOS-Ocean. First, the properties of two different pressure distributions are examined: a flat-top Gaussian pressure distribution, which can represent a broader spatial extent, is derived from the standard Gaussian distribution; the mathematical characteristics of the hyperbolic-tangent pressure distribution are discussed and compared with those of the Gaussian distribution, revealing that the hyperbolic-tangent distribution covers an even wider effective area than the flat-top Gaussian.

On this basis, two main aspects are investigated. On one hand, the influence of grid resolution in HOS-Ocean on the pressure distribution shape and Kelvin wave pattern is explored. For the 3.60 GHz Intel Core i7-9700 single-core processor employed here, when the number of grids is too small (e.g. 128×64), the computational results can lose accuracy; when the number of grids is larger than 1024×1024, the computation tends to diverge. A moderate grid resolution (e.g. 256 × 256) is shown to adequately capture both the geometric features of the pressure distribution and the dominant wave components. Regarding the description of the pressure distribution, for the DTMB5415 hull considered in this paper, which has a ship length L_s of 142 m, a beam B_s of 18.9 m, and a draft D_s of 6.16 m, a grid resolution of approximately 32 points along the ship length and 10 points across the beam is found to be sufficient to capture the primary features of the pressure distribution used in this study and generate a reasonably accurate Kelvin wake pattern. For other hull forms, the grid parameters can be adjusted flexibly based on the configuration presented in this work, provided that the adjusted resolution satisfies the prerequisite of capturing the key features of the pressure distribution and the dominant components of the wave system. This aspect, however, requires more systematic investigation in future work. Furthermore, the effect of the selected free-surface sub-region on the power spectral density of the wake is preliminarily examined. It is observed that a representative power spectrum, which captures the essential features of the wake, can be obtained as long as the selected region covers the main part of the wave system, without requiring the inclusion of the entire computational domain.

On the other hand, a method for determining the draft of each distribution by matching the displacement mass is provided. The influence of different pressure distributions and different drafts on the Kelvin wake is compared and analyzed. The free-surface elevation of the wave field increases with increasing draft. For the DTMB5415 hull considered in this study, when a Gaussian pressure distribution ($n = 2,4$) is applied, the results show slight differences whether the draft is determined by matching displacement mass or is directly set as the physical ship draft. In contrast, when a hyperbolic tangent pressure distribution is used, noticeable discrepancies arise between these two approaches. This suggests that Gaussian pressure distributions may be better suited for describing slender hull forms like the one examined here, whereas hyperbolic tangent distributions might be more appropriate for fuller hull forms—though this would require further systematic investigation. Finally, Kelvin wakes corresponding to different Froude numbers are computed. The comparison demonstrates that, compared with the standard Gaussian distribution, both the flat-top Gaussian and the hyperbolic-tangent distributions produce more pronounced bow and stern wave systems, and the minimum Froude number required to generate a discernible Kelvin wake is lower for these two distributions than for the standard Gaussian.

In future work, several issues require attention. In particular, the rapid attenuation of far-field transverse waves deserves further investigation, and a more detailed analysis of the underlying wave-evolution mechanisms will be considered in future work. The computational instability due to inadequate high-frequency filtering could be addressed by improving the filtering logic in HOS-Ocean or involving the use of more powerful computational resources. Moreover, while smooth pressure distributions allowed moderate grids here, more complex shapes with sharp gradients would demand higher grid resolution and greater computational cost. Techniques such as local grid refinement or overset grids may be worth further exploration.

CRediT authorship contribution statement

Pengju Bao: Writing – original draft, Formal analysis, Data curation. **Mingxing Ren:** Resources, Methodology, Investigation. **Yuan Zhuang:** Writing – review & editing, Funding acquisition, Conceptualization. **Decheng Wan:** Supervision, Funding acquisition, Conceptualization.

Author declarations

Authors have no conflict of interest to declare.

Declaration of competing interest

The authors declare that they have no known competing financial interests or personal relationships that could have appeared to influence the work reported in this paper.

Acknowledgements

This work was supported by the National Natural Science Foundation of China (52571359, 52131102), to which the authors are most grateful.

Appendix A. Distance between the two shoulders of hyperbolic tangent distribution

Taking the longitudinal shape function of the hyperbolic tangent pressure distribution in Eq. (18) as an example, under the condition that the peak remains nearly unity (i.e., $\alpha_{xs} = \alpha_x L_s \geq 6$), determining the shoulder width is equivalent to solving for the distance between the two points where the function value equals $S_H(x)$. That is, two points x_1 and x_2 must satisfy $S_H(x_1) = S_H(x_2) = S_H(x)$, where $0 < S_H(x) < S_H(0) \approx 1$. Since the function is symmetric about $x = 0$, we have $x_2 = -x_1$. Assuming $x_1 > 0$, the equation to solve is:

$$(\tanh(\alpha_x(x+L_s/2)) - \tanh(\alpha_x(x-L_s/2))) = 2S_H(x) \tag{40}$$

let $\alpha_x(x+L_s/2) = \theta_1$ and $\alpha_x(x-L_s/2) = \theta_2$, and then the left-hand side of Eq. (40) can be written as follows:

$$\tanh(\theta_1) - \tanh(\theta_2) = \frac{e^{\theta_1} - e^{-\theta_1}}{e^{\theta_1} + e^{-\theta_1}} - \frac{e^{\theta_2} - e^{-\theta_2}}{e^{\theta_2} + e^{-\theta_2}} = \frac{2\left(e^{\theta_1-\theta_2} - e^{-(\theta_1-\theta_2)}\right)}{\left(e^{\theta_1} + e^{-\theta_1}\right)\cdot\left(e^{\theta_2} + e^{-\theta_2}\right)} = \frac{\frac{e^{\theta_1-\theta_2} - e^{-(\theta_1-\theta_2)}}{2}}{\frac{e^{\theta_1}+e^{-\theta_1}}{2}\cdot\frac{e^{\theta_2}+e^{-\theta_2}}{2}}$$

$$= \frac{\frac{e^{\theta_1-\theta_2} - e^{-(\theta_1-\theta_2)}}{2}}{\frac{e^{\theta_1+\theta_2}+e^{-(\theta_1+\theta_2)}}{4} + \frac{e^{\theta_1-\theta_2}+e^{-(\theta_1-\theta_2)}}{4}} = \frac{\sinh(\theta_1-\theta_2)}{\frac{\cosh(\theta_1+\theta_2)}{2} + \frac{\cosh(\theta_1-\theta_2)}{2}} \tag{41}$$

by substituting Eq. (41) into Eq. (40), one can obtain:

$$\cosh(\theta_1+\theta_2) = \sinh(\theta_1-\theta_2)/S_H(x) - \cosh(\theta_1-\theta_2) \tag{42}$$

and then Eq. (42) becomes:

$$\cosh(2\alpha_x x) = \sinh(\alpha_x L_s)/S_H(x) - \cosh(\alpha_x L_s) \tag{43}$$

$$2\alpha_x x = \pm\,\mathrm{arccosh}(\sinh(\alpha_x L_s)/S_H(x) - cosh(\alpha_x L_s)) \tag{44}$$

The above equation corresponds to Eq. (20). Given that $\alpha_{xs} = \alpha_x L_s \geq 6$, it is reasonable to approximate $\sinh(\alpha_x L_s) \approx e^{\alpha_x L_s}/2$ and $\cosh(\alpha_x L_s) \approx e^{\alpha_x L_s}/$

2. Substituting these approximations into Eq. (44) yields:

$$|x| \approx \frac{1}{2\alpha_x}\operatorname{arccosh}\left(\frac{e^{\alpha_x L_s}}{2}\left(\frac{1}{S_H(x)}-1\right)\right) \tag{45}$$

Based on the definition of the inverse hyperbolic cosine function, $\operatorname{arccosh}(x) = ln\left(x+\sqrt{x^2-1}\right)$. For large values of x, the approximation $\operatorname{arccosh}(x) \approx ln(2x)$ holds. In Eq. (45), the term $\frac{e^{\alpha_x L_s}}{2}\left(\frac{1}{S_H(x)}-1\right)$ is substantially large; therefore, Eq. (45) becomes:

$$|x| \approx L_s \Big/ 2\cdot\left(1+\frac{1}{\alpha_{xs}}\ln\left(\frac{1-S_H(x)}{S_H(x)}\right)\right) \tag{46}$$

The above equation corresponds to Eqs. (21) and (22).

Appendix B. Spatial integral of pressure distribution

Based on Eq. (31) and taking the spatial integral of the longitudinal shape function I_x as an example, the spatial integrals of the Gaussian pressure distribution (Eq. (32)) and the hyperbolic tangent pressure distribution (Eq. (36)) are derived as follows.

1.1. Gaussian pressure distribution

For the standard Gaussian distribution given by Eq. (13), we start from the known definite integral:

$$\int_{-\infty}^{+\infty} e^{-x^2/c^2}\mathrm{d}x = c\sqrt{\pi} \tag{47}$$

where c is a constant.

Let the longitudinal shape function be

$$S_G(x) = e^{-\beta_x\cdot|x/L_s|^{n_x}} \tag{48}$$

For the case $n_x = 2$ (the standard Gaussian), set

$$\frac{\beta_x}{L_s^2}x^2 = \frac{x^2}{c^2} \quad\Longrightarrow\quad c = \frac{L_s}{\sqrt{\beta_x}}. \tag{49}$$

Hence,

$$I_x = \int_{-\infty}^{+\infty} S_G(x)\,\mathrm{d}x = \int_{-\infty}^{+\infty} e^{-\beta_x(x/L_s)^2}\,\mathrm{d}x = \frac{L_s}{\sqrt{\beta_x}}\sqrt{\pi}. \tag{50}$$

$$I\_G = I_x\cdot I_y = \frac{L_s B_s}{\sqrt{\beta_x\beta_y}}\pi \tag{51}$$

For the more general case, where n_x is any real number greater than or equal to 2, and based on symmetry (presence of absolute value sign):

$$I_x = \int_{-\infty}^{+\infty} e^{-\beta_x\cdot|x/L_s|^{n_x}}\,\mathrm{d}x = 2\int_{0}^{+\infty} e^{-\beta_x\cdot(x/L_s)^{n_x}}\,\mathrm{d}x \tag{52}$$

Introduce substitution, set $\delta = \beta_x\cdot(x/L_s)^{n_x}$, and then $x = L_s\cdot(\delta/\beta_x)^{1/n_x}$, and then one can obtain:

$$\mathrm{d}x = \frac{1}{n_x}\cdot\beta_x^{-1/n_x}\delta^{\frac{1}{n_x}-1}\mathrm{d}\delta \tag{53}$$

by substituting Eq. (53) into Eq. (52), we have:

$$I_x = \frac{2L_s}{n_x\beta_x^{1/n_x}}\int_{0}^{+\infty}\delta^{\frac{1}{n_x}-1}\cdot e^{-\delta}\mathrm{d}\delta \tag{54}$$

According to the definition of the Gamma function, namely $\Gamma(\xi) = \int_0^{+\infty} x^{\xi-1}e^{-x}dx, \xi > 0$, then Eq. (54) can be expressed as:

$$I_x = \frac{2L_s}{n_x\beta_x^{1/n_x}}\Gamma\left(\frac{1}{n_x}\right) \tag{55}$$

Using the recursive formula of the gamma function, $\Gamma(\xi+1) = \xi\cdot\Gamma(\xi)$, then $\frac{1}{n_x}\Gamma\left(\frac{1}{n_x}\right) = \Gamma\left(\frac{1}{n_x}+1\right)$.

Subsequently,

$$I_x = \frac{2L_s}{\beta_x^{1/n_x}} \Gamma\left(\frac{1}{n_x} + 1\right) \tag{56}$$

Then we can obtain an expression consistent with Eq. (32).

$$I_G = I_x \cdot I_y = \frac{4L_s B_s}{\beta_x^{1/n_x} \beta_y^{1/n_y}} \Gamma\left(\frac{1}{n_x} + 1\right) \Gamma\left(\frac{1}{n_y} + 1\right) \tag{57}$$

1.2. Hyperbolic tangent pressure distribution

For the hyperbolic tangent pressure distribution, the longitudinal shape function is:

$$S_H(x) = 0.5 \cdot (\tanh(\alpha_x(x + L_s/2)) - \tanh(\alpha_x(x - L_s/2))) \tag{58}$$

Its spatial integral is:

$$I_x = \int_{-\infty}^{+\infty} S_H(x)\, dx = \int_{-\infty}^{+\infty} 0.5 \cdot (\tanh(\alpha_x(x + L_s/2)) - \tanh(\alpha_x(x - L_s/2)))\, dx \tag{59}$$

The antiderivative of the hyperbolic tangent function is $\int \tanh(x) dx = \ln(\cosh(x)) + c$, where c is a constant, so Eq. (59) becomes:

$$I_x = \frac{1}{2\alpha_x} \left[\ln\left(\frac{\cosh(\alpha_x(x + L_s/2))}{\cosh(\alpha_x(x - L_s/2))} \right) \right]_{-\infty}^{+\infty} \tag{60}$$

Let $\alpha_x(x + L_s/2) = \theta_1$ and $\alpha_x(x - L_s/2) = \theta_2$. When $x \longrightarrow +\infty$, $\cosh(\theta_1) = \frac{e^{\theta_1} - e^{-\theta_1}}{2} \longrightarrow \frac{e^{\theta_1}}{2}$, and $\cosh(\theta_2) = \frac{e^{\theta_2} + e^{-\theta_2}}{2} \longrightarrow \frac{e^{\theta_2}}{2}$ and then $\ln\left(\frac{\cosh(\theta_1)}{\cosh(\theta_2)}\right) \longrightarrow \ln(e^{\theta_1 - \theta_2}) = \alpha_x L_s$; similarly, when $x \longrightarrow -\infty$, $\cosh(\theta_1) = \frac{e^{\theta_1} - e^{-\theta_1}}{2} \longrightarrow \frac{e^{-\theta_1}}{2}$, and $\cosh(\theta_2) = \frac{e^{\theta_2} + e^{-\theta_2}}{2} \longrightarrow \frac{e^{-\theta_2}}{2}$ and then $\ln\left(\frac{\cosh(\theta_1)}{\cosh(\theta_2)}\right) \longrightarrow \ln(e^{-\theta_1 + \theta_2}) = -\alpha_x L_s$. Hence, Eq. (60) becomes:

$$I_x = \frac{1}{2\alpha_x} (\alpha_x L_s - (-\alpha_x L_s)) = L_s \tag{61}$$

Then we can obtain an expression consistent with Eq. (36).

$$I_H = I_x \cdot I_y = L_s \cdot B_s \tag{62}$$

Data availability

The data that support the findings of this study are available from the corresponding author upon reasonable request.

References

Arnold-Bos, A., Martin, A., Khenchaf, A., 2007. Obtaining a ship's speed and direction from its Kelvin wake spectrum using stochastic matched filtering. 2007 IEEE International Geoscience and Remote Sensing Symposium 1106–1109. https://doi.org/10.1109/IGARSS.2007.4422995.

Bao, P., Ren, M., Huang, F., Wan, D., Zhuang, Y., 2025. Numerical simulation of wide-area Kelvin's ship wake based on high-order spectral method. Phys. Fluids 37 (12), 122139. https://doi.org/10.1063/5.0308308.

Bao, P., Zhuang, Y., Wan, D., 2026. Kelvin wake induced by an improved Gaussian pressure distribution based on high order spectral method. Proceedings of the thirty-sixth (2026) International Ocean and Polar Engineering Conference submitted for publication.

Benzaquen, M., Darmon, A., Raphaël, E., 2014. Wake pattern and wave resistance for anisotropic moving disturbances. Phys. Fluids 26 (9), 092106. https://doi.org/10.1063/1.4896257.

Brard, R., 1972. The representation of a given ship form by singularity distributions when the boundary condition on the free surface is linearized | journal of ship research | OnePetro. J. Ship Res. 16 (1), 79–92.

Chen, X.B., 1999. An Introductory Treatise on ship-motion Green Functions. Proc. 7th Intl Conf. on Num. Ship Hydro. Nantes (France) 1999 (pp. 1-21).

Chen, X., Zhu, R., Song, Y., Fan, J., 2019. An investigation on HOBEM in evaluating ship wave of high speed displacement ship. J. Hydrodyn. 31 (3), 531–541. https://doi.org/10.1007/s42241-018-0092-8.

Chester, C., Friedman, B., Ursell, F., 1957. An extension of the method of steepest descents. Math. Proc. Camb. Phil. Soc. 53 (3), 599–611. https://doi.org/10.1017/S0305004100032655.

Colen, J., Kolomeisky, E.B., 2021. Kelvin–Froude wake patterns of a traveling pressure disturbance. Eur. J. Mech. B Fluid 85, 400–412. https://doi.org/10.1016/j.euromechflu.2020.10.008.

Dam, K.T., Tanimoto, K., Fatimah, E., 2008. Investigation of ship waves in a narrow channel. J. Mar. Sci. Technol. 13 (3), 223–230. https://doi.org/10.1007/s00773-008-0005-6.

Darmon, A., Benzaquen, M., Raphaël, E., 2014. Kelvin wake pattern at large Froude numbers. J. Fluid Mech. 738, R3.

Dawson, C.W., 1977. A Practical Computer Method for Solving ship-wave Problems, pp. 30–38.

Dempwolff, L.C., Melling, G., Windt, C., Lojek, O., Martin, T., Holzwarth, I., Bihs, H., Goseberg, N., 2022. Loads and effects of ship-generated, drawdown waves in confined waterways—A review of current knowledge and methods. Journal of Coastal and Hydraulic Structures. https://doi.org/10.48438/JCHS.2022.0013.

Doctors, L.J., 1993. On the use of pressure distributions to model the hydrodynamics of air-cushion vehicles and surface-effect ships. Nav. Eng. J. 105 (2), 69–89. https://doi.org/10.1111/j.1559-3584.1993.tb02264.x.

Doctors, L.J., Sharma, S.D., 1972. The wave resistance of an air-cushion vehicle in steady and accelerated motion. J. Ship Res. 16 (4), 248–260. https://doi.org/10.5957/jsr.1972.16.4.248.

Dommermuth, D.G., Yue, D.K.P., 1987. A high-order spectral method for the study of nonlinear gravity waves. J. Fluid Mech. 184, 267–288. https://doi.org/10.1017/S002211208700288X.

Ducrozet, G., Bonnefoy, F., Le Touzé, D., Ferrant, P., 2016. HOS-ocean: Open-source solver for nonlinear waves in open ocean based on High-Order Spectral method. Comput. Phys. Commun. 203, 245–254. https://doi.org/10.1016/j.cpc.2016.02.017.

Ertekin, R.C., Webster, W.C., Wehausen, J.V., 1986. Waves caused by a moving disturbance in a shallow channel of finite width. J. Fluid Mech. 169, 275–292. https://doi.org/10.1017/S0022112086000630.

Forbes, L.K., 1989. An algorithm for 3-dimensional free-surface problems in hydrodynamics. J. Comput. Phys. 82 (2), 330–347. https://doi.org/10.1016/0021-9991(89)90052-1.

Fouques, S., Pákozdi, C., 2020. A mixed eulerian-lagrangian High-Order Spectral method for the propagation of ocean surface waves over a flat bottom. J. Comput. Phys. 8, 100071. https://doi.org/10.1016/j.jcpx.2020.100071. X.

Gadd, G., 1976. A Method of Computing the Flow and Surface Wave Pattern Around Full Forms, 18. Royal Institution of Naval Architects, pp. 207–219.

Gomit, G., Rousseaux, G., Chatellier, L., Calluaud, D., David, L., 2014. Spectral analysis of ship waves in deep water from accurate measurements of the free surface

elevation by optical methods. Phys. Fluids 26 (12), 122101. https://doi.org/10.1063/1.4902415.
Gouin, M., Ducrozet, G., Ferrant, P., 2017. Propagation of 3D nonlinear waves over an elliptical mound with a high-order Spectral method. Eur. J. Mech. B Fluid 63, 9–24. https://doi.org/10.1016/j.euromechflu.2017.01.002.
Gramstad, O., Johannessen, T.B., Lian, G., 2023. Long-term analysis of wave-induced loads using high order spectral method and direct sampling of extreme wave events. Mar. Struct. 91, 103473. https://doi.org/10.1016/j.marstruc.2023.103473.
Guyenne, P., 2017. A high-order spectral method for nonlinear water waves in the presence of a linear shear current. Computers & Fluids 154, 224–235. https://doi.org/10.1016/j.compfluid.2017.06.004. ICCFD8.
Havelock, T.H., 1908. The propagation of groups of waves in dispersive media, with application to waves on water produced by a travelling disturbance. Proc. R. Soc. Lond. - Ser. A Contain. Pap. a Math. Phys. Character 81 (549), 398–430. https://doi.org/10.1098/rspa.1908.0097.
He, J., Zhang, C., Zhu, Y., Zou, L., Li, W., Noblesse, F., 2016. Interference effects on the Kelvin wake of a catamaran represented via a hull-surface distribution of sources. Eur. J. Mech. B Fluid 56, 1–12. https://doi.org/10.1016/j.euromechflu.2015.10.009.
Honger, E., 1923. A contribution to the theory of Ship waves. Arkiv För Matematik, Astronomi och Fysik utgivet av K. Svenska vetenskapsakademien 12 (17).
Kelvin, L., 1887. On ship waves. Proc. Inst. Mech. Eng. 38 (1), 409–434.
Kirezci, C., Babanin, A.V., Chalikov, D.V., 2021. Modelling rogue waves in 1D wave trains with the JONSWAP spectrum, by means of the high order spectral method and a fully nonlinear numerical model. Ocean Eng. 231, 108715. https://doi.org/10.1016/j.oceaneng.2021.108715.
Kotchin, N., 1951. On the wave-making resistance and lift of bodies submerged in water. Tech. & Research Bull.
Liang, H., Chen, X., 2018. Asymptotic analysis of capillary–gravity waves generated by a moving disturbance. Eur. J. Mech. B Fluid 72, 624–630. https://doi.org/10.1016/j.euromechflu.2018.08.012.
Liang, H., Chen, X., 2019. Viscous effects on the fundamental solution to ship waves. J. Fluid Mech. 879, 744–774. https://doi.org/10.1017/jfm.2019.698.
Liang, H., Li, Y., Chen, X., 2024. An Earth-fixed observer to ship waves. J. Fluid Mech. 984, A14. https://doi.org/10.1017/jfm.2024.167.
Lighthill, M.J., 1978. Waves in Fluids. Cambridge University Press.
Lindenmuth, W., Ratcliffe, T., Reed, A., 1991. Comparative Accuracy of Numerical Kelvin Wake Code Predictions—'Wake off, 275.
Lo, P.H.-Y., 2021. Approximate ship wake solution for fast computation. Ocean Eng. 235, 109405. https://doi.org/10.1016/j.oceaneng.2021.109405.
Ma, C., Zhu, Y., Wu, H., He, J., Zhang, C., Li, W., Noblesse, F., 2016. Wavelengths of the highest waves created by fast monohull ships or catamarans. Ocean Eng. 113, 208–214. https://doi.org/10.1016/j.oceaneng.2015.12.042.
Moisy, F., Rabaud, M., 2014. Scaling of far-field wake angle of nonaxisymmetric pressure disturbance. Phys. Rev. 89 (6), 063004. https://doi.org/10.1103/PhysRevE.89.063004.
Noblesse, F., 1977. The fundamental solution in the theory of steady motion of a ship. J. Ship Res. 21 (2), 82–88. https://doi.org/10.5957/jsr.1977.21.2.82.
Noblesse, F., Yang, C., 2007. Elementary water waves. J. Eng. Math. 59 (3), 277–299. https://doi.org/10.1007/s10665-006-9115-5.
Paprota, M., 2023. A fourier Galerkin method for ship waves. Ocean Eng. 271, 113796. https://doi.org/10.1016/j.oceaneng.2023.113796.
Pethiyagoda, R., McCue, S.W., Moroney, T.J., 2014. What is the apparent angle of a Kelvin ship wave pattern? J. Fluid Mech. 758, 468–485.
Pethiyagoda, R., Moroney, T.J., Lustri, C.J., 2021. Kelvin wake pattern at small Froude numbers. J. Fluid Mech. 915, A216.
Rabaud, M., Moisy, F., 2013. Ship wakes: Kelvin or Mach Angle? Phys. Rev. Lett. 110 (21), 214503.
Scarpa, G.M., Zaggia, L., Manfè, G., Lorenzetti, G., Parnell, K., Soomere, T., Rapaglia, J., Molinaroli, E., 2019. The effects of ship wakes in the Venice Lagoon and implications for the sustainability of shipping in coastal waters. Sci. Rep. 9 (1), 19014. https://doi.org/10.1038/s41598-019-55238-z.
Sun, Y.-X., Liu, P., Jin, Y.-Q., 2018. Ship wake components: isolation, reconstruction, and characteristics analysis in spectral, spatial, and TerraSAR-X image domains. IEEE Trans. Geosci. Rem. Sens. 56 (7), 4209–4224. https://doi.org/10.1109/TGRS.2018.2828833.
Ursell, F., 1960. On Kelvin's ship-wave pattern. J. Fluid Mech. 8 (3), 418–431. https://doi.org/10.1017/S0022112060000700.
West, B.J., Brueckner, K.A., Janda, R.S., 1987. A new numerical method for surface hydrodynamics—West—1987—Journal of Geophysical Research: Oceans—Wiley Online Library. J. Geophys. Res. 92 (11), 803–811.
Yao, J., Bingham, H.B., Zhang, X., 2023. Nonlinear effects of variable bathymetry and free surface on mini-tsunamis generated by a moving ship. Phys. Rev. Fluids 8 (9), 094801. https://doi.org/10.1103/PhysRevFluids.8.094801.
Yao, J., Bingham, H.B., Zhang, X., 2024. The influence of static versus dynamic pressure distribution strategies for modelling nonlinear waves generated by ships. J. Fluid Mech. 997, A70. https://doi.org/10.1017/jfm.2024.741.
Zaggia, L., Lorenzetti, G., Manfé, G., Scarpa, G.M., Molinaroli, E., Parnell, K.E., Rapaglia, J.P., Gionta, M., Soomere, T., 2017. Fast shoreline erosion induced by ship wakes in a coastal lagoon: field evidence and remote sensing analysis. PLoS One 12 (10), e0187210. https://doi.org/10.1371/journal.pone.0187210.
Zakharov, V.E., 1972. Stability of periodic waves of finite amplitude on the surface of a deep fluid. J. Appl. Mech. Tech. Phys. 9 (2), 190–194. https://doi.org/10.1007/BF00913182.
Zhang, C., He, J., Zhu, Y., Yang, C.-J., Li, W., Zhu, Y., Lin, M., Noblesse, F., 2015. Interference effects on the Kelvin wake of a monohull ship represented via a continuous distribution of sources. Eur. J. Mech. B Fluid 51, 27–36. https://doi.org/10.1016/j.euromechflu.2014.12.006.
Zheng, Z.-Q., Zou, L., Zou, Z.-J., 2023. A numerical study of passing ship effects on a moored ship in confined waterways with new benchmark cases. Ocean Eng. 280, 114643. https://doi.org/10.1016/j.oceaneng.2023.114643.
Zhu, Y., He, J., Wu, H., Li, W., Noblesse, F., 2018. Basic models of farfield ship waves in shallow water. J. Ocean Eng. Sci. 3 (2), 109–126. https://doi.org/10.1016/j.joes.2018.04.003.
Zhu, Y., He, J., Zhang, C., Wu, H., Wan, D., Zhu, R., Noblesse, F., 2015. Farfield waves created by a monohull ship in shallow water. Eur. J. Mech. B Fluid 49, 226–234. https://doi.org/10.1016/j.euromechflu.2014.09.006.